JGR Space Physics

RESEARCH ARTICLE
10.1029/2021JA029695

Topside Measurements at Jicamarca During the 2019–2020 Deep Solar Minimum

S. Derghazarian[1], D. L. Hysell[1], and R. H. Varney[2]

[1]Earth and Atmospheric Sciences, Cornell University, Ithaca, NY, USA, [2]SRI International, Menlo Perk, CA, USA

Key Points:

- New Jicamarca ISR topside measurements of the 2019–2020 solar minimum are presented
- ISR comparison with DMSP and with ICON for first time at very low solar flux shows consistency and provides insight into predawn heating
- Comparisons between ISR and SAMI2-PE model outputs reveals new insight into composition and energetics of topside

Correspondence to:

S. Derghazarian,
sd779@cornell.edu

Citation:

Derghazarian, S., Hysell, D. L., & Varney, R. H. (2021). Topside measurements at Jicamarca during the 2019–2020 deep solar minimum. *Journal of Geophysical Research: Space Physics*, *126*, e2021JA029695. https://doi.org/10.1029/2021JA029695

Received 18 JUN 2021
Accepted 22 OCT 2021

Abstract We present measurements of the equatorial topside ionosphere above Jicamarca made during extremely low solar flux conditions during the deep solar minimum of 2019–2020. Measurements were made in October, 2019, February, 2020, and September, 2020. The main features observed are a large and extended decrease in noontime temperatures unlike that seen in studies at moderate solar flux levels, predawn ionospheric heating as early as 0300 LT, large day-to-day variability in the O^+/H^+ transition height, and negligible helium ion concentration at all altitudes. Data from the Ion Velocity Meter (IVM) instrument onboard the Ionospheric Connection Explorer (ICON) and the Topside Ionospheric Plasma Monitor (SSIES) onboard the Defense Meteorological Satellite Program (DMSP) satellites are used to assess agreement with ISR data and assist with the analysis of the predawn heating phenomena. We also analyze the data in light of the SAMI2-PE model which shows less agreement with the data than at higher solar flux. The main areas of discrepancy with the data are outlined, such as the absence of significant predawn heating, less pronounced decreases in noontime temperatures, and much higher O^+ fractions at high altitudes, particularly in September. Finally, a sensitivity analysis of the model to various forcing agents such as neutral winds, plasma drifts, solar flux, and heat flow is performed. A discussion is presented on bridging the discrepancies in future model runs. Novel techniques of clutter removal and noise power bias correction are introduced and described in the appendices.

1. Introduction

This study is an analysis of the equatorial F-region and topside ionosphere during the recent deep solar minimum of 2019–2020 using incoherent scatter measurements from the Jicamarca Radio Observatory. This period marks the transition between two solar cycles with solar flux levels comparable to those of the deep minimum of 2008–2009 and among the weakest in recorded history. The current study complements an earlier one (Hysell et al., 2009) which details an experiment conducted in May, 2008, at moderately low solar flux with hardware capabilities and signal processing techniques that follow those described in (Hysell et al., 2015), along with some recent upgrades.

The topside is defined as that part of the ionosphere between the F2 peak and the protonobase, with the latter situated at 2,000 km at its lowest point (Banks et al., 1976; Hysell et al., 2015). In this region of the upper atmosphere, lower densities result in increased mean free paths, and transport becomes increasingly important in relation to chemistry. Diffusion dominates in the form of ambipolar diffusion, meridional wind induced drifts along B, and $E \times B$ drifts (Schunk and Nagy, 2009). In addition, field aligned photoelectrons travel from lower altitudes at off-equatorial regions toward the equatorial topside heating thermal electrons along the way, which then transfer the energy to ions in their vicinity. These photoelectrons are produced in the bottomside F1 region where photochemistry dominates.

The properties of the topside are strongly influenced by drifts and meridional winds. Zonal electric fields couple with the geomagnetic field to produce vertical $E \times B$ drifts which convect ions upwards or downwards depending on the time of day. Meridional winds can influence temperature, densities and composition in the topside by redistributing plasma along field lines between the equatorial ionization anomaly (EIA) and the topside (Varney, 2012). Having accurate drift and wind estimates is an essential ingredient for ionospheric models to reproduce realistic densities, temperatures, and ion composition. The most commonly used drift model at the magnetic equator is the Fejer-Scherliess model (Scherliess and Fejer, 1999) which however has limitations in periods of extremely low solar flux. A study performed using Communication/Navigation Outage Forecast System (C/NOFS) satellite data by (Klenzing et al., 2011; Pfaff et al., 2010) found unique features during the previous deep

solar minimum that are not captured in the model such as downward afternoon drifts and the near absence of a preversal enhancement in some cases.

In addition to drifts and winds, the most significant process responsible for heating the topside ionosphere is the transport of energetic electrons along field lines resulting in the transfer of energy to local thermal electrons and an increase in the ambient plasma temperature. The production of energetic electrons increases proportionally to solar EUV radiation. The $F_{10.7}$ solar flux is a commonly used proxy for solar radiation but its appropriateness in calculating ionization and EUV heating rates has been questioned when the solar flux is very low (Heelis et al., 2009). The authors state that direct observations of the EUV spectrum and the O^+/H^+ transition height, which is a good indicator of the intensity of the solar flux (MacPherson et al., 1998; Heelis et al., 2009), reveals that the heating rates during this period should be much lower than those estimated using the solar flux index. The study by Heelis et al. (2009) mapped the transition height in detail for low latitudes during the 2008 solar minimum using measurements from the C/NOFS satellite and found that it varies between 450 km in the nighttime to 850 km in the daytime at its highest point.

The presence of H^+, one the main ion constituents of the topside, can be traced back to neutral H composition in the lower atmosphere which is itself produced by the photodissociation of hydrogen containing molecules of tropospheric origin such as methane (Kockarts, 2002). The H^+ ions are generated through resonant charge exchange with O^+ and increasingly become the dominant ion constituent with altitude. The NRLMSISE-00 (Mass Spectrometer Incoherent Scatter Radar) model (Picone et al., 2002) provides neutral density measurements used in ionospheric models. However, a study by Waldrop and Paxton (2013) emphasizes the uncertainty in values of neutral H in the MSIS model by factors of up to two. The authors argue that in situ composition data acquired over three decades ago did not include direct H measurements. Instead, H was inferred through oxygen density measurements under the assumption of an unproven chemical equilibrium in the thermosphere (Brinton et al., 1975; Waldrop et al., 2006).

A phenomenon referred to as morning overshoot or predawn heating (conjugate photoelectron heating) has been reported in several topside studies and is well established by decades of observations (Carlson, 1966, 1968; Kakinami et al., 2010). It is commonly understood to occur when photoelectrons stream along magnetic field lines from the sunlit hemisphere to the darker hemisphere, contributing to increases in electron temperature before local sunrise (Oyama, Balan, et al., 1996; Oyama, Watanabe, et al., 1996). Studies performed by Stolle et al. (2011) using the CHAMP satellite and subsequently by Yang et al. (2020) using SWARM and ISS instrumentation revealed that morning overshoot temperatures reach a maximum at the magnetic equator, a phenomenon which cannot be explained using conjugate photoelectron transport theory. Most surprisingly, predawn heating was observed as early as 0300 LT by SWARM-B (which orbits at 520 km) at the dip equator and at equinox during the 2008 solar minimum. This is considerably earlier than the arrival of the first photoelectrons due to conjugate transport. Similarly, at midlatitudes above the Arecibo observatory during October of 2008 and 2009, heating took place around 0300 LT at an altitude of approximately 480 km which is an hour earlier than photoelectron conjugate transport (Aponte et al., 2013). The origin of this phenomenon is not yet known but one could speculate about a connection with airglow emissions. Excitation of far-ultraviolet twilight airglow in the 135.6 nm and 137–154 nm bands around the terminator was measured using data from the GOLD satellite (Solomon, 2017; Solomon et al., 2020) and shown in the figures of (Solomon et al., 2020). The observations revealed the airglow to be spread zonally with gradually decreasing intensity, up to 5° to the west of the terminator, during the 2008 solar minimum in the months of June, October, and December. Although shorter wavelengths in the EUV range which are capable of photoionizing oxygen were not part of this study, an older study by (Chakrabarti, 1984) presented data from the EUV spectrometer on board the U.S. Air Force STP78-1 satellite in which emissions of 91 nm were detected with intensities ranging from 80 to 100 Rayleighs. Other sources of predawn far-ultraviolet radiation are geocoronal emissions of Lyman-α. This phenomenon occurs through resonant scattering of solar Lyman-α radiation from neutral H ions in the exosphere (Zoennchen et al., 2015). The wavelength of the emissions is 121.6 nm, and although present at nighttime and before sunrise, their energy falls below the ionization threshold of all major ionospheric constituents, rendering them incapable of generating photoelectrons required for topside heating. In addition to Lyman-α, a study by (Strobel et al., 1974) presents NRL sounding rocket data on the nighttime ionosphere that reveals the presence of Lyman-β emissions, He I and He II lines. The authors describe the origin of these emissions as terrestrial (Hydrogen and Helium geocorona) and interplanetary sources.

These terms are included in the SAMI2 model for nighttime photoionization, and their impact on predawn heating will be evaluated later in this study.

The hybrid long pulse/double pulse incoherent scatter radar experiments described in this paper were conducted to provide insight into the topside ionosphere at three different time periods during the 2019–2020 deep solar minimum. We first describe the experimental methods employed including recent improvements to the signal processing techniques. Estimates of ionospheric parameters are then presented along with comparisons to satellite data. In the discussion section, the SAMI2-PE ionospheric model is used to analyze the data and the influence of the various forcing agents described above through sensitivity analyses. Finally, a discussion is presented on how to resolve lingering discrepancies between the model and the data.

2. Experimental Methodology

The data are analyzed according to the methods described in (Hysell et al., 2015, 2009) with a few changes. Estimates of N_e, T_e, T_i, H^+, and He^+ are obtained using a full-profile approach (Holt et al., 1992; Lehtinen et al., 1996). The forward model is based on ISR theory for magnetized ionospheric plasmas at small magnetic aspect angles incorporating Coulomb collisions (Sulzer & Gonzalez, 1999; Milla & Kudeki, 2006) and predicts lag product profiles from state parameter profiles in view of the instrument function of the Jicamarca radar. The inversion algorithm for the full-profile analysis technique estimates the parameters by reducing the discrepancy between model predictions and measured lag products, and is regularized using 10 different cost functions. Some of these pertain to physical restrictions, and others ensure the suppression of unphysical oscillations in the parameter estimates.

For the experiments described in this manuscript, the hybrid long pulse/double pulse Faraday (Farley 1969; Pingree, 1990) experiment was used. This consists of the transmission of a 1.6 ms (240 km) long pulse on a single circular polarization followed by pairs of 100 μs (15 km) short pulses with staggered lags and alternating circular polarization (Hysell et al., 2015). The double pulse pairs are separated by n times 200 μs, with values of n ranging from 0 to 10. The second pulse is inverted to help suppress cross-talk as described in (Pingree, 1990). The interpulse period used was 40 ms. Sampling takes place on two receivers at a rate of 40 kHz, but additional digital boxcar filtering is applied that reduces the sampling interval to 100 μs. The integration time of the experiment is 11.2 min. Each transmitter can deliver 1 MW of power limited only by a 6% duty cycle, which is underutilized in the experiment.

The double pulse Faraday rotation experiment has been employed at Jicamarca since the early days to estimate ISR autocorrelation functions while providing absolute electron density estimates (Farley, 1969; Pingree, 1990). Each polarization excites a distinct magnetoionic mode (ordinary or extraordinary) of the plasma and ensures that clutter from uncorrelated ranges (including clutter from the electrojet (Forbes, 1981; Hoymork et al., 2000) and the so-called 150-km echoes (Balsley, 1964; Chau & Kudeki, 2006)) is minimized. The relatively short width of each pulse gives it fine range resolution but provides a lower SNR and fewer lag-product estimates per unit time than the long pulse. The double pulse technique is useful for probing altitudes from the valley region through the F-peak but is impractical in the topside where the signal strength is inadequate.

Estimates of the plasma auto-correlation function (ACF) are produced with this technique for each range gate from incoherently integrated voltage autocorrelation measurements which are constructed by combining individual lag product measurements. In contrast to the long pulse technique, the analysis is gated, and every range gate is treated independently. A pure oxygen atmosphere is assumed which allows the zero crossing point to be converted into a T_e estimate and the depth of the ACF into an estimate of the T_e/T_i ratio (Farley et al., 1967). Both of these provide initial temperature guesses to the ACF fitting routine which utilizes a Levenberg–Marquardt based algorithm.

The density estimates from the double pulse data are not absolute and need to be calibrated using Faraday rotation. This occurs when the polarization plane of a linearly polarized wave (a combination of left and right circular polarizations) rotates due to a difference in phase between the return signals from each mode. This difference is caused by a dissimilarity in the refraction indices which are wave dependent and this difference is proportional to the electron density. Measuring this value using the zero lags of the double pulse data provides a technique for

obtaining absolute electron density estimates. The Faraday rotation derived density profiles are used as a reference for fitting the double pulse power profiles using a least squares approach.

Self clutter is eliminated through the use of the orthogonal polarizations and signals contaminated from ground clutter or the equatorial electrojet (EEJ; Forbes, 1981; Hoymork et al., 2000) are automatically rejected by comparing the measurements from both the receivers.

The long pulses are transmitted using a single circular polarization with 1 MW of power per transmitter employed and with a negligeable power droop (Hysell et al., 2017). Although samples were acquired at a rate of 40 kHz, digital boxcar filtering for the long pulse experiment reduces the sampling interval to 50 μs, still twice the rate used in previous experiments (e.g., Hysell et al., 2015). This change allows twice the number of lag products to be calculated per pulse (Whereas we previously acquired 16 lags in 1.6 ms, we now acquire 16 lags in 800 μs and neglect longer lags which have lag products close to zero). The change was introduced to improve experimental performance which suffers during periods of extremely low solar flux but will be retained in experiments going forward. Range gates are spaced by 15 km intervals.

Data from the long pulse are analyzed using the full-profile algorithm similar to the one described in (Holt et al., 1992; Lehtinen et al., 1996). The receiver samples are stochastic in nature, and the information about ionospheric state parameters is contained in the second order statistics of the data. Lag products for each range gate and their associated variances are calculated from the long pulse receiver samples and averaged by incoherently integrating a total of 14,300 samples over a period of 11.2 min. Only error variances are used for the error analysis instead of the full covariance matrix since doing so is not expected to alter the results significantly (Huuskonen & Lehtinen, 1996).

Theoretical plasma autocorrelation functions are subsequently tabulated using the theory for magnetized ionospheric plasmas at small magnetic aspect angles mentioned earlier and specified at discrete ranges spaced by 15 km intervals and at 16 lags spaced by 50 μs. Two dimensional range-lag ambiguity functions (Lehtinen & Huuskonen, 1996; Nygrén, 1996) are then computed using the methods describe. They represent the radar instrument functions which transform plasma autocorrelation values into measurable lag products and act as averaging kernels combining multiple autocorrelation measurements into individual lag products. They are computed only once at the beginning of the experiment and reused throughout.

An important consideration is the dependence of the backscatter gain on the magnetic aspect angle within the scattering volume. The Jicamarca two-way radiation pattern has a beamwidth of ≈1°, with the main axis forming an angle of ≈4° in the northern direction with respect to the dip equator at an altitude of 500 km (see Figure 1). The effect of variations in magnetic aspect angle across the beam is usually not considered. For this work, however, lag products were calculated incorporating the effect. A Gauss-Hermite interpolation scheme was used as described by (Hysell et al., 2015). In addition, IGRF coefficients (Alken et al., 2021) were updated to the 13th edition released in December, 2019, and valid from 1900 to 2025. This is especially important given the recent, rapid migration of the geomagnetic equator.

Initial estimates or guesses of N_e, T_e, T_i, and H^+ profiles are specified at a limited number of discrete points and transformed into cubic splines that allow interpolation at the same altitudes as the experimental range gates. Temperature and composition initial guesses are simple parametrized sigmoid functions inspired by previous experimental results whereas the density estimates are constructed by fitting long pulse power estimates to those obtained by Faraday calibrated double-pulse power estimates, with the full procedure described. The interpolated points are then transformed first into plasma autocorrelation functions and then into lag product estimates using the ambiguity function. An iterative optimization procedure based on the Levenberg–Marquardt scheme (Levenberg, 1944; Marquardt, 1963) is then used to find the parameter profile curves that minimize the discrepancy with measured lag products with regularization based on the cost functions described earlier.

The choice of a good initial guess is critical for the optimization algorithm and even more so when the solar flux and associated signal-to-noise ratio are very low. Performance was improved by cycling through a larger family of curves in a grid search using four parametrized functions instead of three as in previous experiments (Hysell et al., 2015). The curve with the lowest combination of chi-square and L_∞ norms was chosen for the initial guess. The addition of the L_∞ norm to the standard chi-square metric was to ensure lag product estimates at higher altitudes did not deviate excessively from the lag product measurements. In the interest of execution time and

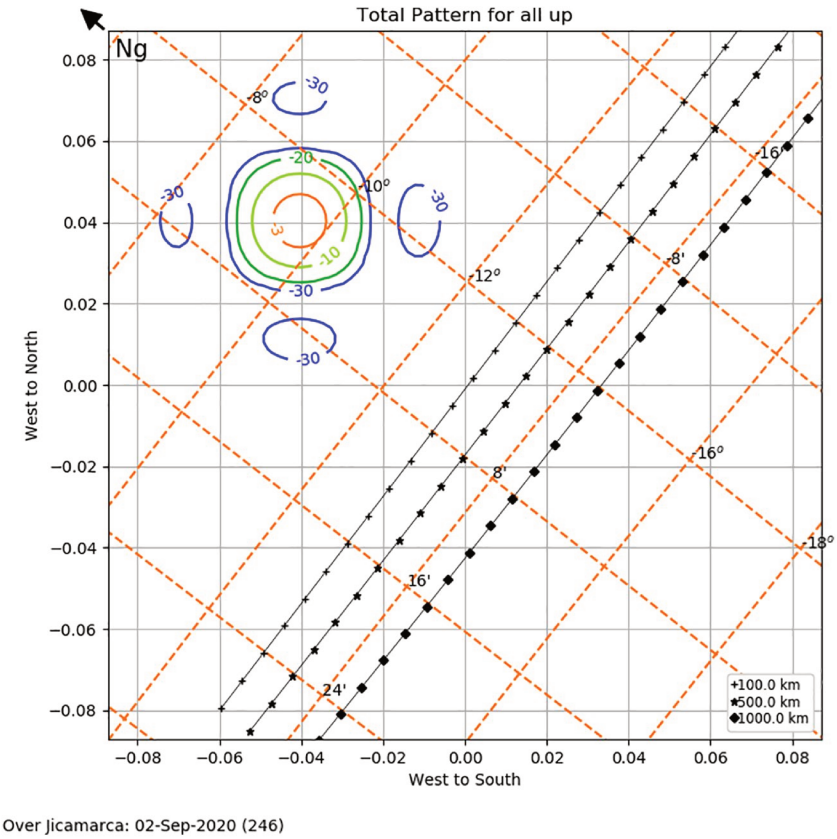

Figure 1. Antenna pattern for Jicamarca ISR transmitter. The black lines represent the loci of perpendicularity for altitudes of 100, 500, and 1,000 km from left to right respectively. North is indicated in the upper left corner, and declination and hour angle values (in minutes) are indicated in the figure on the dotted orange lines. The main beam represented in the figure is centered at 9.52° south and 0.8° west.

efficiency, the traditional grid search is replaced with the Optuna (Akiba et al., 2019) stochastic optimization algorithm.

Noise samples were measured during transmitter off periods following 128 continuous pulse transmissions and were acquired using the same filters used for the remaining experiment. A 100 μs digital boxcar filter was used. Noise power was calculated by squaring voltage samples during the transmitter off periods, and then stored to be later subtracted from the zero lag of the signal. We can track when the galaxy is overhead by looking at the peak in the noise power corresponding to maximum sky noise temperatures for the given day. On September 2, the Milky Way galaxy is overhead post-sunset around 2000 LT, on October 15 this occurs around 1,700 LT, and on February 18 it takes place at 0900 LT. Poor performance of the algorithm can be expected at these times because of the greatly lowered SNR (Hysell et al., 2017).

To remove clutter generated by satellites and coherent echoes, order statistics is used. Sixteen consecutive lag product averages corresponding each to 0.6 s of experimental time are ranked in ascending order, with the first and last two values rejected in the calculation of the sample mean. Since the beam transit time of satellite debris lasts a few seconds only (Hysell, 2000), lag products from contaminated voltage samples would automatically become outliers and get rejected. The same procedure is applied to noise samples. It should be noted that the technique works well only for clutter with brief transit times and would not be effective against longer lived sources such as that caused by geosynchronous satellites (Hysell, 2000).

The clutter removal technique can introduce a bias in the sample mean depending on the skewness of the underlying distribution, which may need be corrected. If the underlying statistics are normally distributed, then rejecting samples on both ends of the distribution would not be expected to introduce a bias. It is instructive to remember that summing a large number of random variables together causes the distribution to tend to a normal

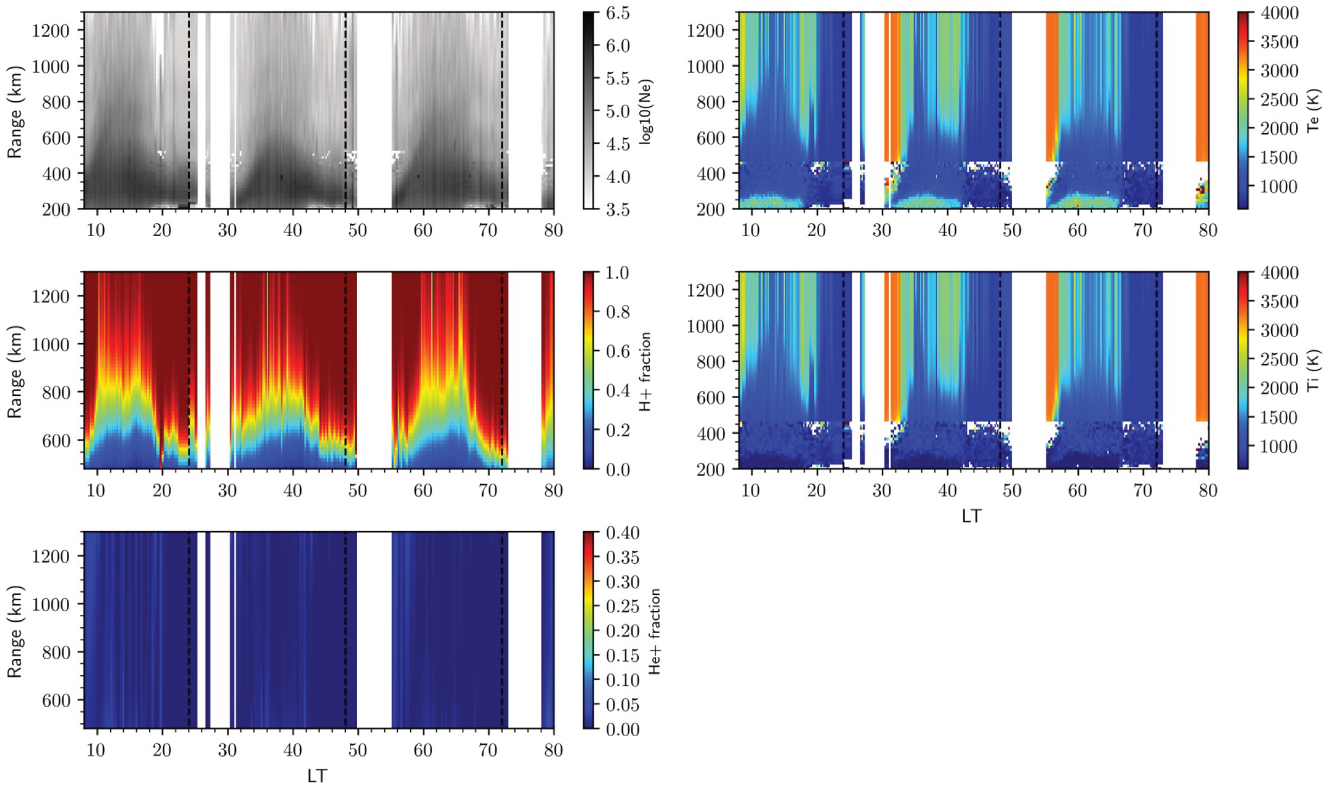

Figure 2. Incoherent scatter measurements for September 1–4, 2020. Measurements were taken at very low solar flux with an average $F_{10.7}$ flux of 70. Panels on the left show (from top down) N_e, H^+ fraction and He^+ fraction respectively, and panels on the right show T_e (top) and T_i (bottom). White space indicates missing data. Predawn heating can be observed in a thin time strip around 0300 LT on September 2 (2,700 LT on the Figure). Black vertical dashed lines indicate change in day.

one according to the central limit theorem (Papoulis, 1984). In the case of lag products, single values calculated by individual voltage samples have complicated distributions mentioned in Appendix B. However, because 128 consecutive values are added together, the distribution has little skewness. This is not the case for noise samples. Individual samples follow a gamma distribution but only 22 consecutive samples are added which does not reduce the skewness of the original distribution sufficiently to forego the need for bias correction. A full explanation of the underlying bias correction technique is given in Appendix A and B although the formulas mentioned are not applied explicitly for processing noise power values in this study. A temporary generic constant is used throughout each experiment to correct the noise estimate bias, similar to the technique used in Hysell et al., 2015. Incorporating the more extensive noise correction technique mentioned in the Appendix remains to be addressed.

The main beam of the antenna is steered a few degrees off-perpendicular with a declination of −9.52°, in a northern direction with respect to the dip equator. This is different than the traditional position used in the previous experiment at moderate solar flux (Hysell et al., 2015) where the main beam was oriented with a declination of −14.56° in a southern direction with respect to the magnetic equator. Recently, some upgrades have also been made to the antenna. Partial electronic beam steering has been installed. Spark-gaps were removed and replaced with solid-state T/R switches. The transmitters drivers were updated.

3. Results

Experiments were conducted on October 15 and 16, 2019, February 17 and 19, 2020, and September 1 and 4, 2020. The data are illustrated in Figures 2–4. The solar flux was extremely low during all three campaigns with an average $F_{10.7}$ of 66 during the October experiment, 69 during the February experiment, and 70 during the September experiment. This translates into low signal-to-noise ratio as densities are lower and backscatter is weaker. The SNR drops below unity at lower altitudes than usual. For example, at 1500LT, this occurs around 585 km in the October experiment, and around 675 km in both the February and September experiments. At 1,000 km for

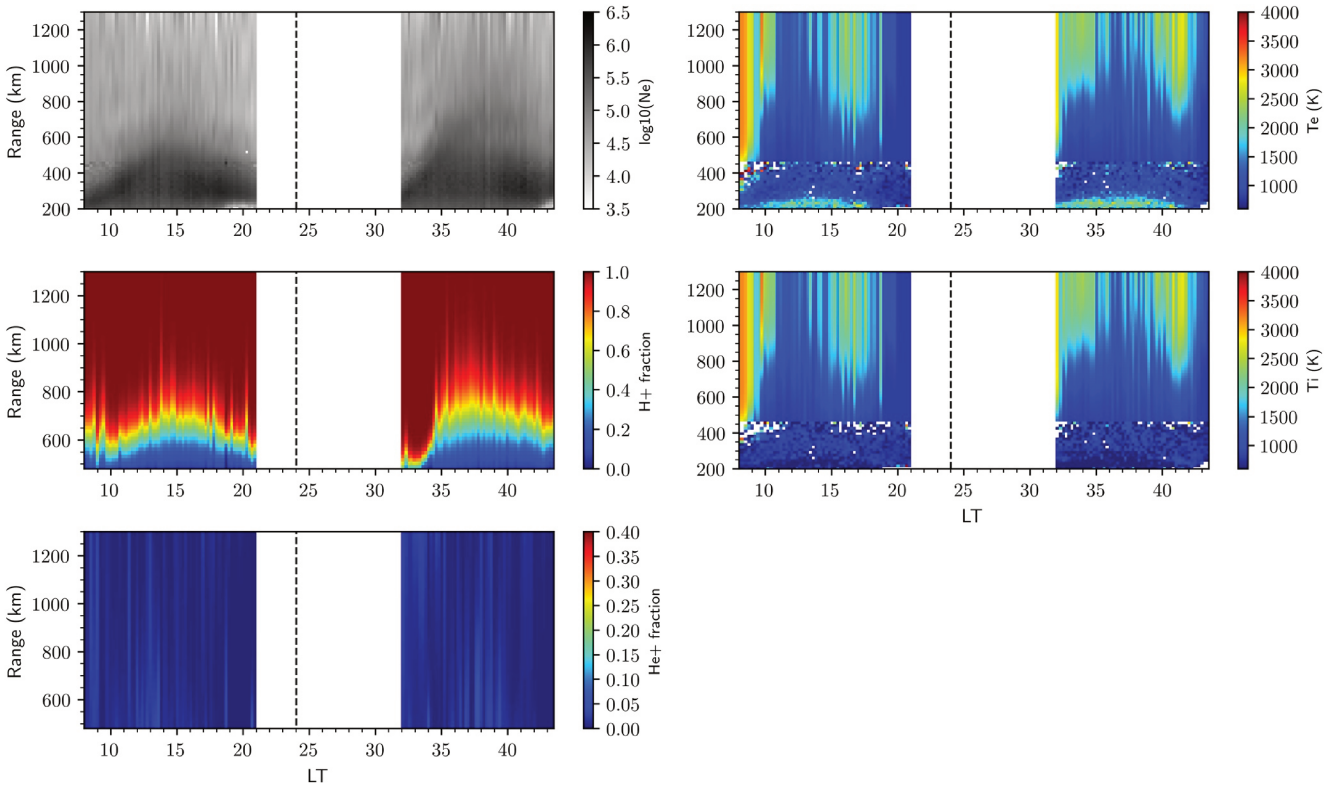

Figure 3. Similar to Figure 2 but for October 15 and 16, 2019. The average solar flux is at one of its lowest values for the solar minimum with an average $F_{10.7}$ of 66. Plots indicate N_e, T_e, T_i, H^+ fraction and He^+ fraction. Black vertical dashed lines indicate change in day.

the same local time, the SNR is less than 0.03 in October and 0.1 in both September and February. This results in large uncertainties in the estimated parameters at higher altitudes and the fitting is primarily influenced by lower altitude data.

During most of the predawn, sunrise, and portions of the post-sunset period, areas corresponding to data gaps are grayed out in the relevant plots. The recovery of ionospheric parameters during these periods was not feasible due to increased clutter from equatorial spread-F (ESF; Farley et al., 1970) generated coherent echoes and satellite debris causing both Faraday rotation and double pulse estimates to break down. ESF was more severe during the times of this experiment than during previous studies at solar minimum (see JULIA Drift plots on JRO Madrigal for 2008 data and digital high frequency plots for 2019–2020 found on the Jicamarca Radio Observatory website).

Early morning ion temperatures in SAMI2-PE were found to be in reasonably good agreement with those measured by the IVM instrument onboard the Ionospheric Connection Explorer (ICON) and were used to set an upper ceiling for temperature values in the full-profile analysis, to prevent temperature extremes due to ESF contaminated data.

Some of the key characteristics of the data are:

1. The O^+/H^+ transition height varies significantly from one day to the next in all three datasets and the maximum altitude appears to be positively correlated with density values in the topside. There is no consistent morphology from one day to the next unlike sawtooth patterns which appeared at more moderate solar flux.
2. The day-to-day variability in densities is significant during all three months. This is unlike previous studies at low solar flux and at moderate solar flux, which revealed much fewer changes. Unusually low densities are observed above 400 km on February 19, 2020 (Figure 4) and the values show little diurnal variation which is a feature not seen on any other day. Additionally, on February 18, the density reaches a maximum in time at 1,900 LT (4,300 LT in Figure) for a fixed altitude (in the 500–800 km range) which is a unique feature not seen on other days.

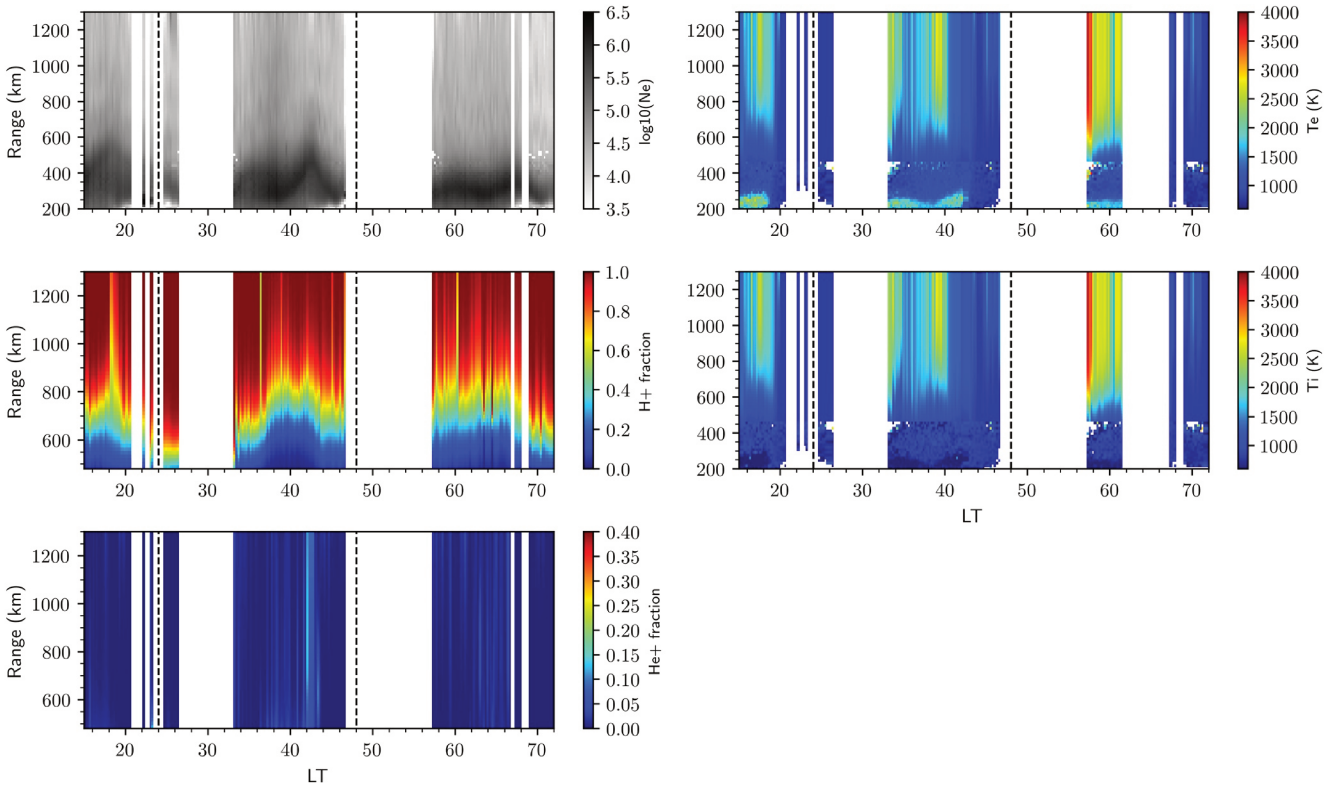

Figure 4. Similar to Figure 2 but for February 17–20, 2020. The average value of $F_{10.7}$ was 69. Plots indicate N_e, T_e, T_i, H^+ fraction and He^+ fraction. Similar to 2. Black vertical dashed lines indicate change in day. The appearance of a bright vertical line in the He^+ plot can be ruled out as an artifact.

3. All of the datasets exhibit a temperature maximum in the early morning, followed by a sharp decrease between 0800 and 0900 LT with temperatures continuing to drop throughout the afternoon before increasing again from 1,500 LT onwards and reaching a second peak around 1,800 LT. From 1,800 LT to 1,900 LT, there is another sharp decline in temperature before it reaches close to its minimum value around 2,000 LT. The large drop in temperatures observed around noon extends from 600 km to the topmost altitudes measured. The longest and steepest noontime drop occurs during the month with the lowest average solar flux which is on October 15, 2019. This is a feature seen on June 11, 2008 and at moderate solar flux (Hysell et al., 2015) although the minimum temperatures reached are higher. Another interesting observation is that of higher than normal temperatures on February 19, 2020 compared to all other days due to the uniquely lower densities.
4. Predawn heating is observed around 0300 LT on September 2, 2020 (2,700 LT in 2).
5. The presence of He^+ is negligible in the data and does not appear in distinct layers as in previous experiments at moderate solar flux (Hysell et al., 2015).

Another feature of the observed O^+/H^+ transition height is that it appears to decrease with the solar flux. In October 2019, when the solar flux is at its lowest, this height is at a mere 700 km at its highest point in the daytime and 500 km at night. This matches very closely with measurements taken during the previous topside study at low solar flux in June 2008. In February 2020, the daytime peak transition height reaches 750 and 650 km at night whereas in September 2020 the maximum height in the daytime is at 750 and 550 km at night. The daytime values in this study are in general considerably lower than those measured at moderate solar flux (Hysell et al., 2015).

A comparison between satellite and ISR measurements on September 2, 2020 is shown in Figure 5. Data from the IVM instrument onboard the Ionospheric Connection Explorer (ICON) and the Topside Ionospheric Plasma Monitor (SSIES) onboard the Defense Meteorological Satellite Program (DMSP) are used. The satellites orbit on average at altitudes of 600 and 850 km respectively.

Conjunctions were counted whenever the orbit of the satellite crossed a cube with a magnetic latitude of $0 \pm 5°$, geographic longitude of $-76.87 \pm 5°$ and a geographic altitude of 850 ± 15 km for DMSP and 600 ± 15 km

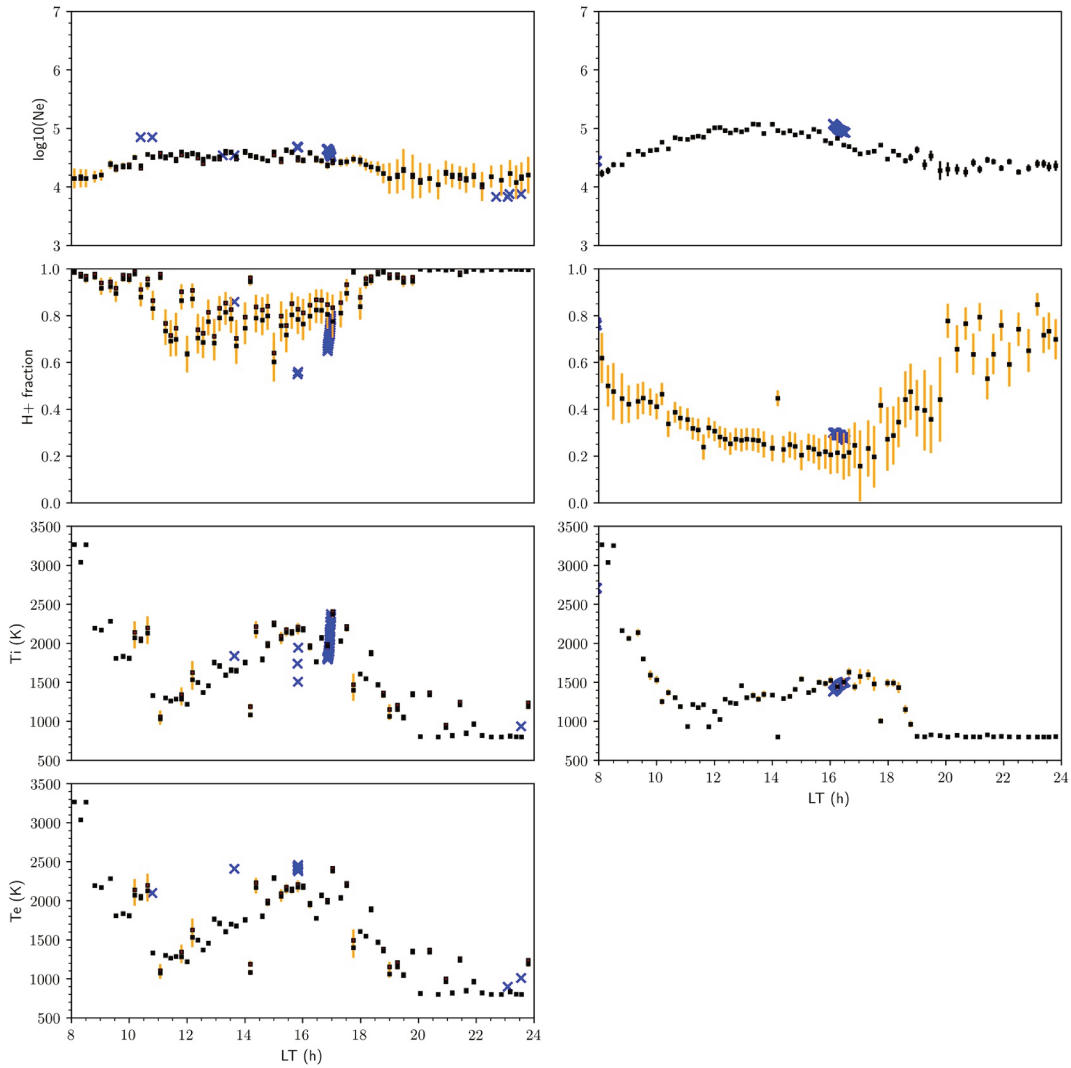

Figure 5. Jicamarca ISR measurements are compared to DMSP and ICON satellite measurements on September 2, 2020. Jicamarca measurements are shown in black with orange error bars, and DMSP and ICON measurements are shown in blue. The four panels in the left column show comparisons of Jicamarca ISR estimated N_e, T_e, T_i, and H^+ with DMSP data, at an altitude of 850 km. The three panels on the right column show comparisons of the same parameters from Jicamarca ISR with ICON data at 600 km. An electron temperature comparison is excluded since it is not measured by ICON instruments.

for ICON. Since the cross-section of this cube is larger than that of the scatter volume of the transmitter, some physical variations in parameters are introduced and thus it is not expected that satellite and ISR data be in perfect agreement. Except for the presence of some outliers, a good deal of agreement can be seen. Error bars were not available but all of the available data that meets the above criteria was plotted in order to be able to visually assess variance.

Predawn heating which is observed in Figure 2 and in the bottom right panel of Figure 10 as early as 0300 LT, occurs ≈1.5 hr before the beginning of photoproduction in the off-equatorial F1 regions intersecting the same field lines above Jicamarca. The time at which photoelectron mediated topside heating begins was estimated by calculating the earliest sunrise times at 300 km altitude on the northern and southern ends of the field lines. This is an estimate of the minimum altitude parallel transport is able to take place (Huba et al., 2000). The aacgmv2 Python package (Shepherd, 2014) based on the AACGM coordinate system (Baker & Wing, 1989; Bhavnani & Hein, 1994; Hein & Bhavnani, 1996; Heres & Bonito, 2007) was used to map field lines, and sunrise times on the 300 km points were calculated according to the expression of the solar zenith angle used in SAMI2. The first vertical dashed line in the bottom right panel in Figure 10 indicates this time which is around 0445 LT, and

demonstrates that standard conjugate transport theory cannot explain the earlier occurrence of predawn heating. Previous studies demonstrate the same phenomenon. The March 2013 plots included in (Hysell et al., 2015) showed heating to occur prior to 0400 LT more than 30 min earlier to that caused by non local photoelectron transport.

4. Theory and Analysis

To analyze the measurements from the previous section, we make use of the SAMI2-PE model (Varney et al., 2012), which is an augmented version of the SAMI2 model (SAMI2 is another model of the ionosphere Huba et al., 2000). SAMI2 solves the five moment transport equations augmented with a heat flow term based on Fourier's law. The chemical and dynamical plasma evolution is solved for seven ion species (H^+, O^+, He^+, O_2^+, NO^+ and N_2^+), and the temperature equation for three: H^+, O^+, He^+. The neutral atmosphere is specified at the beginning of the run with the NRLMSISE-00 (Mass Spectrometer Incoherent Scatter Radar) model (Picone et al., 2002), and the neutral winds with HWM14 (Horizontal Wind Model) by Drob et al. (2015). $E \times B$ drifts are based on the Fejer-Scherliess model (Scherliess & Fejer, 1999).

SAMI2 uses a non-orthogonal grid based on an offset, tilted dipole coordinate system modeled on the geomagnetic field. This system is well suited for modeling ionospheric processes as the components parallel and perpendicular to the magnetic field lines are weakly coupled to each other and can be solved separately. Ion inertial terms are included in the momentum equation which makes the model especially suitable for the topside where collisions are less frequent.

The thermodynamic processes involved in SAMI2 include heating/cooling through electron-neutral and ion-neutral collisions, heating through a photoelectron term, conduction parallel to B, convection perpendicular to B in the transverse direction, and adiabatic expansion/contraction.

Heating of thermal electrons in the topside occurs via collisions with photoelectrons originating in the off-equatorial F1 regions and streaming up field lines. It is captured in the model through the photoelectron heating term of the temperature equation. In SAMI2, photoelectrons are assumed to be generated below 300 km and to propagate upwards along field lines starting at 300 km. The integrated electron density along the field lines along with a non-local heating factor is then used to determine their contribution to the energy balance.

SAMI2-PE includes a more sophisticated kinetic theory based photoelectron transport model that takes into account multiple pitch angle streams, includes the effect of curved magnetic field lines, and uses an energy degradation procedure. Ambient electron heating by photoelectrons and secondary production rates are calculated which are then coupled to the fluid equations in the underlying SAMI2 code. None of the models are expected to reproduce day-to-day variability which would require a data-driven approach.

The SAMI2-PE model was run for the corresponding days and times of the Jicamarca experimental campaigns from October 15 and 16, 2019, February 17–20, 2020, and September 1–4, 2020. In comparison to the study at moderate solar flux (Hysell et al., 2015), the current study reveals a wider discrepancy between model and measurements. This is especially striking in the case of the H^+ fraction and the O^+/H^+ transition height. In most instances, except for morning and night times, the modeled O^+ fractions remain greater than 0.2 even at the highest altitudes while the data indicate near total H^+ at the same location. Temperatures also differ markedly with the model overestimating them in the morning, mid-afternoon, and before sunset, with the most significant disagreement being in the mid-afternoon. This is evident when comparing the measured and modeled plots (Figures 2–8). The bottom right panel of Figure 10 shows this effect clearly at an altitude of 700 km. The black solid line indicates modeled T_e and the black vertical markers indicate measured values. Several areas of discrepancy stand out:

1. The measured predawn temperatures begin to increase as early as 0300 LT in the data whereas this is seen at 0500 LT or later in the model
2. The minimum noontime temperature is lower in the data and occurs at different times in the data and model. For instance, the lowest value in the data occurs around 1100 LT on September 2, 2020, whereas in the model the minimum occurs 3 hr later at 1400 LT and is ≈400 K warmer.
3. The peak in temperatures prior to sunset is around 500 K higher and 1.5 hr earlier than the peak seen in the model after which temperatures drop drastically in the data but more gradually in the model.

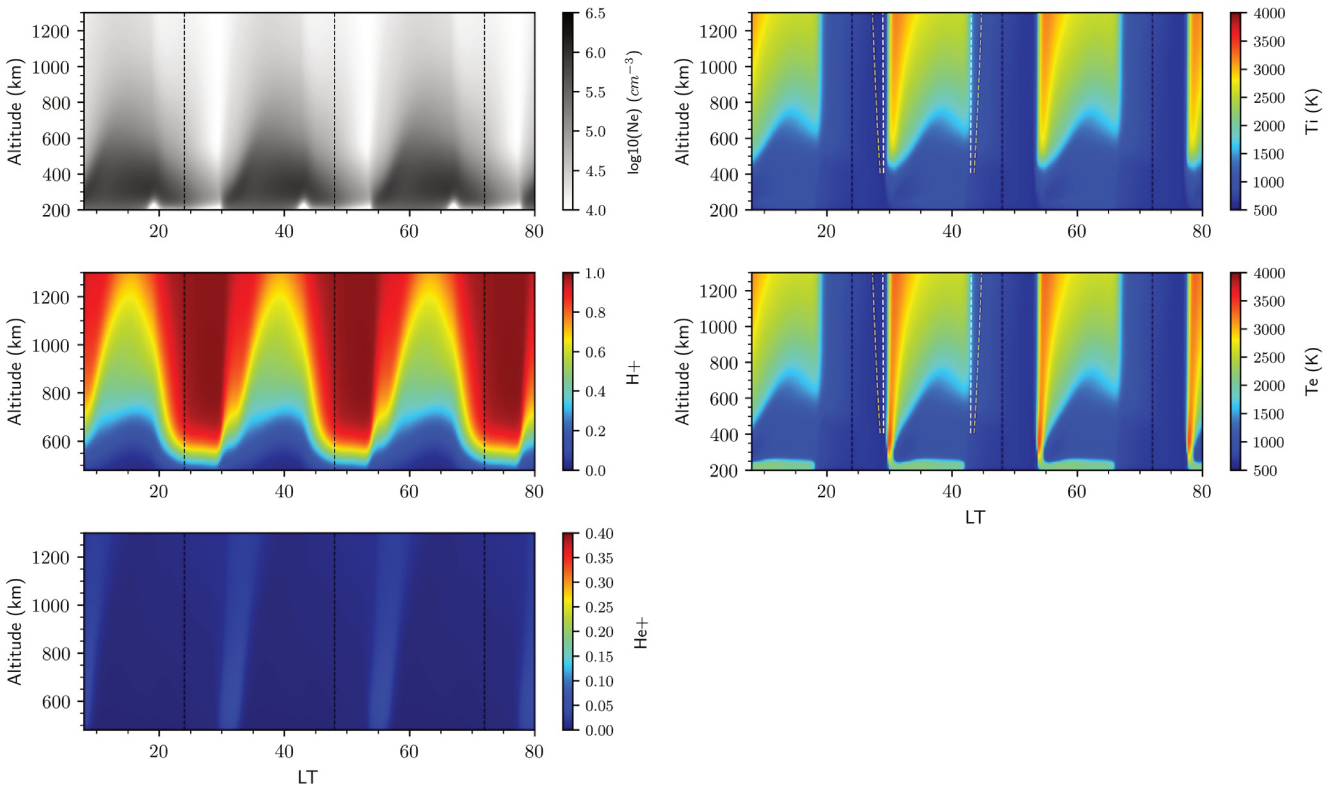

Figure 6. SAMI2-PE model simulations for September 1–4, 2020. Plots indicate N_e, T_e, T_i, H^+ fraction and He^+ fraction. Earliest sunrise and latest sunset times at the 150 km altitude point on field lines passing through the ISR scatter volume are shown by white dotted and nearly vertical lines. The 150 km height represents the altitude corresponding to the photoproduction peak, and corresponds to when temperatures start to increase in the model (even though not apparent in color scale). Slightly tilted yellow dotted lines indicate local sunrise time. Black vertical dashed lines indicate change in day.

4. The O^+/H^+ transition height is higher in the model than in the data for September. For example, on September 2, it is at 900 km whereas it is 750 km in the data.
5. The H^+ fraction is much lower in the model at high altitudes for September but on other months the discrepancies are small.
6. The He^+ fraction in both the model and the measurements is significantly lower than it was during times of higher solar flux (Hysell et al., 2015). Although the modeled He^+ quantities display morphological features with higher values in the morning, measured quantities appear negligible.

A more comprehensive comparison of Jicamarca measurements with SAMI2-PE is displayed in Figure 9. The temperatures show good agreement at night and in the late afternoon but the model temperatures are 500–1,000 K higher than the measurements at other times. Densities show reasonable agreement except at pre-dusk and at night. The H^+ fractions in the model are up to 20% lower than those in the data with the exception of nighttime.

A sensitivity analysis of T_e, N_e, and H^+ is performed and illustrated in the first three panels of Figure 10. The effect of increasing/decreasing the neutral wind, $E \times B$ drifts, neutral H fraction, solar flux, and magnitude of the heat flow vector by different factors is examined followed by the motivation behind these modifications. The effect of these changes on reducing the discrepancies between model and data is also assessed.

The following important features were observed:

1. Doubling the neutral H fraction significantly improves H^+ agreement with data but worsens N_e agreement for altitudes above 700 km.
2. Doubling the neutral winds increases T_e and flattens the mid-afternoon dip instead of deepening it which worsens the temperature agreement. The fit of N_e to data is improved but the discrepancy in H^+ fractions and transition height is increased.
3. Increasing the $E \times B$ drifts has the opposite effect to increasing the neutral winds.

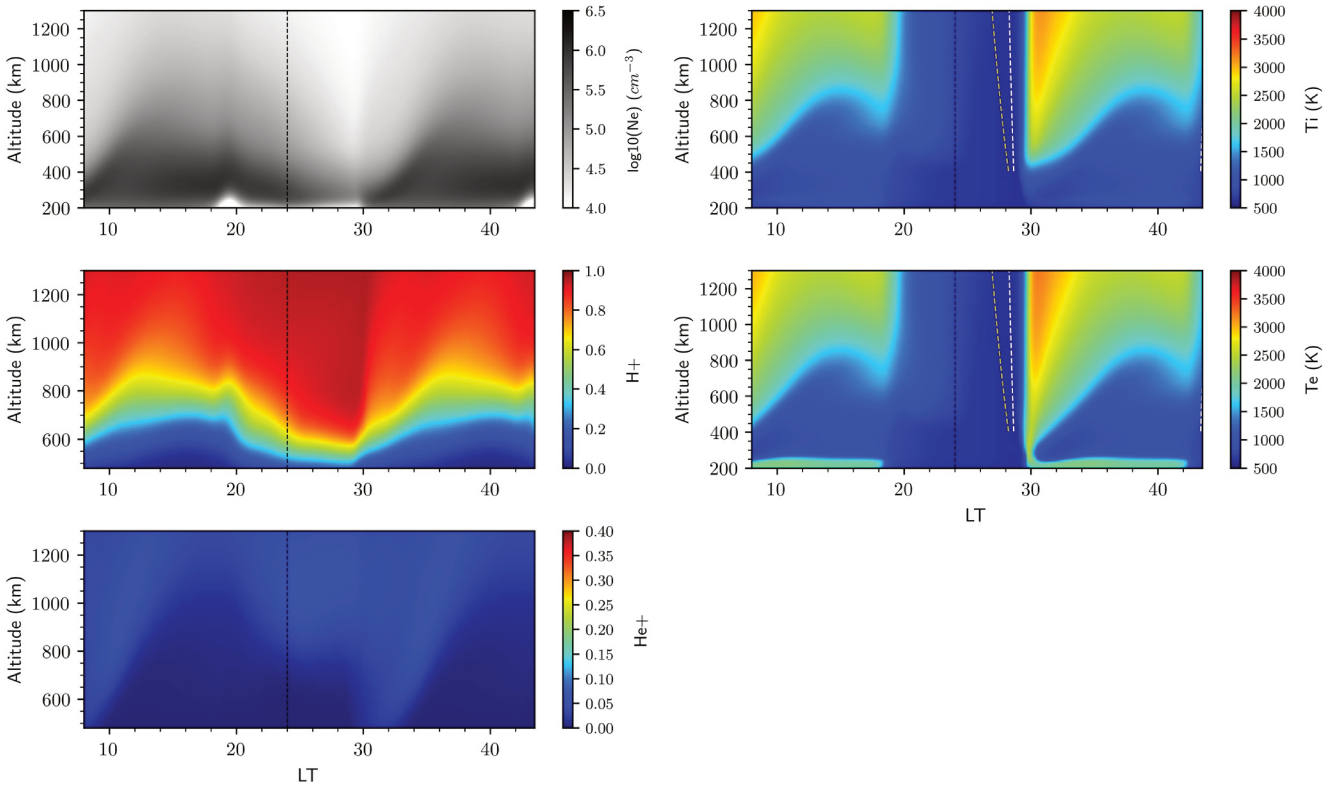

Figure 7. SAMI2-PE model simulations for October 15 and 16, 2019. Plots indicate N_e, T_e, T_i, H^+ and He^+ fraction. Detailed explanation can be found in 6. Black vertical dashed lines indicate change in day.

4. Reducing the solar flux slightly increases temperatures above 400 km, lowers the density and increases the H^+ fraction. The temperature discrepancy is increased but H^+ fraction and N_e agreement is improved.
5. Reducing the magnitude of the electron heat flow vector causes an overall increase in topside temperatures with the greatest effect seen at sunrise and sunset. It does not change the densities or the H^+ fraction much and lessens the mid-afternoon dip in temperature instead of deepening it.
6. Increasing the magnitude of the H^+ heat flow vector by a factor of 10 does not cause any noticeable change in any of the parameters except for a slight increase of temperatures at midday.

In all observations, it is clear that no combination of parameters can easily be found that would cause agreement of data with measurements.

The effect of the electric field was examined because it strongly influences temperatures at noon. Increasing the electric field causes a stronger upward $E \times B$ drift in the afternoon, convecting lower temperature and heavier ions upwards, increasing topside densities and heat capacity, and reducing photoelectron transport efficiency. This results in a general lowering of temperatures. Since the drop in noontime temperatures appears to increase with altitude in the measurements (see Figure 5), it is possible that $E \times B$ drifts increase with altitude. Jicamarca drift plots (available on JRO Madrigal) show that drifts do not vary much with altitude but the data are mostly restricted to 600 km and below. Drift data for higher altitudes would need to be examined and compared to the Fejer-Scherliess model. If it is revealed that drifts do increase with altitude, then the divergence of this drift would contribute not only in lowering temperatures, but would result in a decrease in density at higher altitudes. This could help explain why simply doubling the $E \times B$ drift cannot capture the densities well even though it improves the temperature fit at midday. Data from the IVM instrument on the ICON satellite would be invaluable in this regard and would be useful once drift data are validated.

Thermospheric winds were also analyzed for their strong influence on topside temperatures. They are mostly divergent during the day and multiplying their influence by a factor greater than unity enhances the transport of plasma away from the equatorial regions toward the equatorial anomaly which reduces the density in the topside

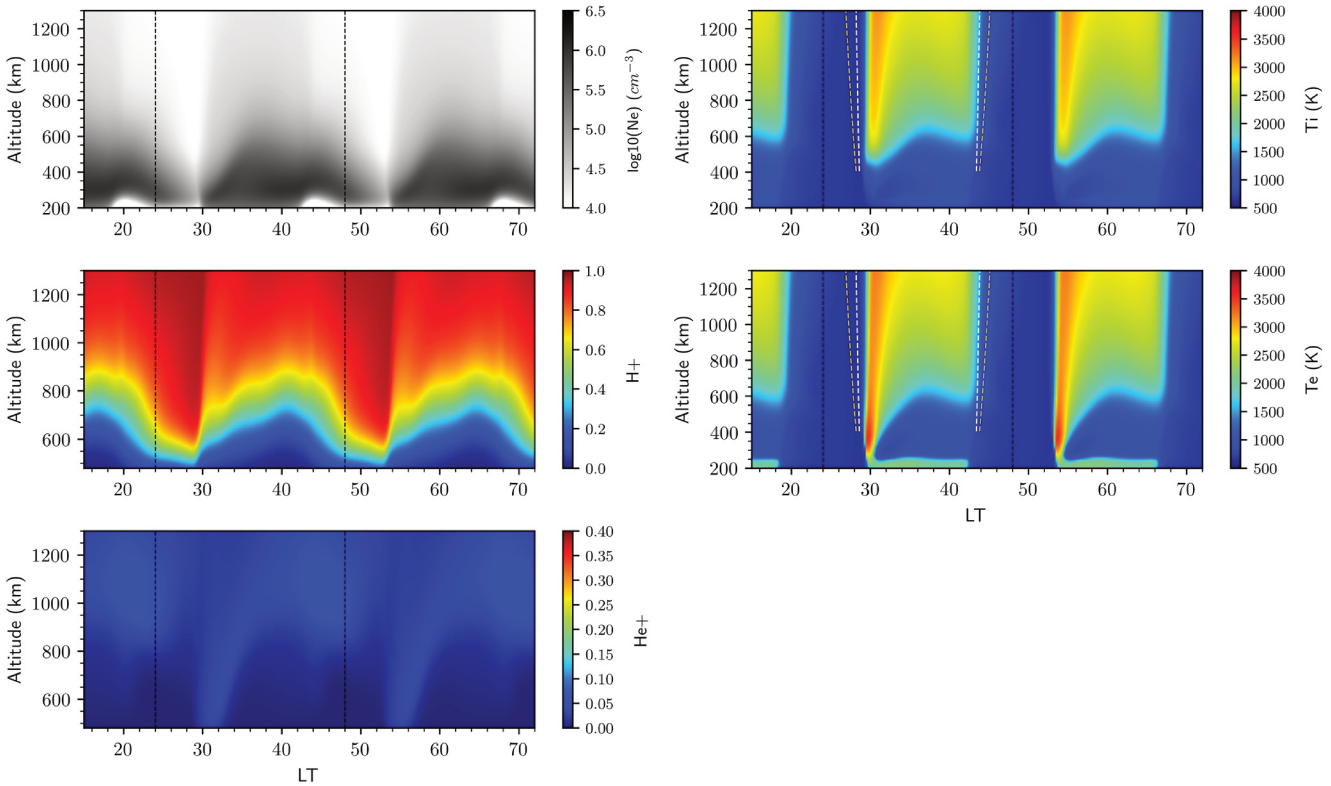

Figure 8. SAMI2-PE model simulations for February 17 and 20, 2020. Plots indicate N_e, T_e, T_i, H^+, and He^+ fraction. Detailed explanation can be found in 6. Black vertical dashed lines indicate change in day.

and causes a decrease in collisional cooling. With these reduced densities, photoelectron heating also becomes more efficient and an overall increase in temperatures takes place. An accurate model is very essential for getting densities and temperatures right. In a similar manner to the drifts, neutral wind data from the Michelson Interferometer for Global High-resolution Thermospheric Imaging instrument (MIGHTI) onboard the ICON satellite could be useful to produce better wind estimates for targeted experimental campaigns.

The $F_{10.7}$ solar radio index (Tapping, 2013) is a good proxy for the solar spectrum intensity but is only a multiplicative factor which does not specify the distribution of individual frequencies in the spectrum. It was lowered in Figure 10 to show its influence on each of the parameters, in particular for increasing the H^+ fraction and lowering the transition height. However, this only emphasizes the need for updating the HEUVAC model with a more recent model such as FISM-P (Chamberlin et al., 2018; Thiemann et al., 2017). Another possibility is to use direct solar spectrum measurements from a satellite such as SDO (Solar Dynamics Observatory) and to insert them into SAMI2. It is likely that either of these approaches would improve parameter agreement with Jicamarca measurements for the days of experimental campaigns.

Examining the effect of increasing H values is motivated by the study of Waldrop and Paxton (2013), mentioned earlier, that brings to light the uncertainty in values of neutral H in the MSIS model by factors of up to two. Increasing the H values at the beginning of the simulation, improves the fit with experimental H^+ values significantly with little impact on other parameters.

Multiplying the magnitude of the heat flow vector(s) by a large/small factor is an attempt to simulate the effect of including a thermoelectric or diffusive thermal term of significant magnitude.

Diffusion thermal terms arise in higher moment transport equations and correspond to induced heat flow due to temperature gradients within or relative drifts between the ion species. In two studies by St. Maurice and Schunk, (1977) and Conrad and Schunk, (1979), the authors examined the minimum interspecies drift required to produce diffusive thermal effects in a two species topside ionosphere composed exclusively of H^+ and O^+ ions. They found that drifts less than 100 m/s in any of the gases can induce significant heat flow in the H^+ gas.

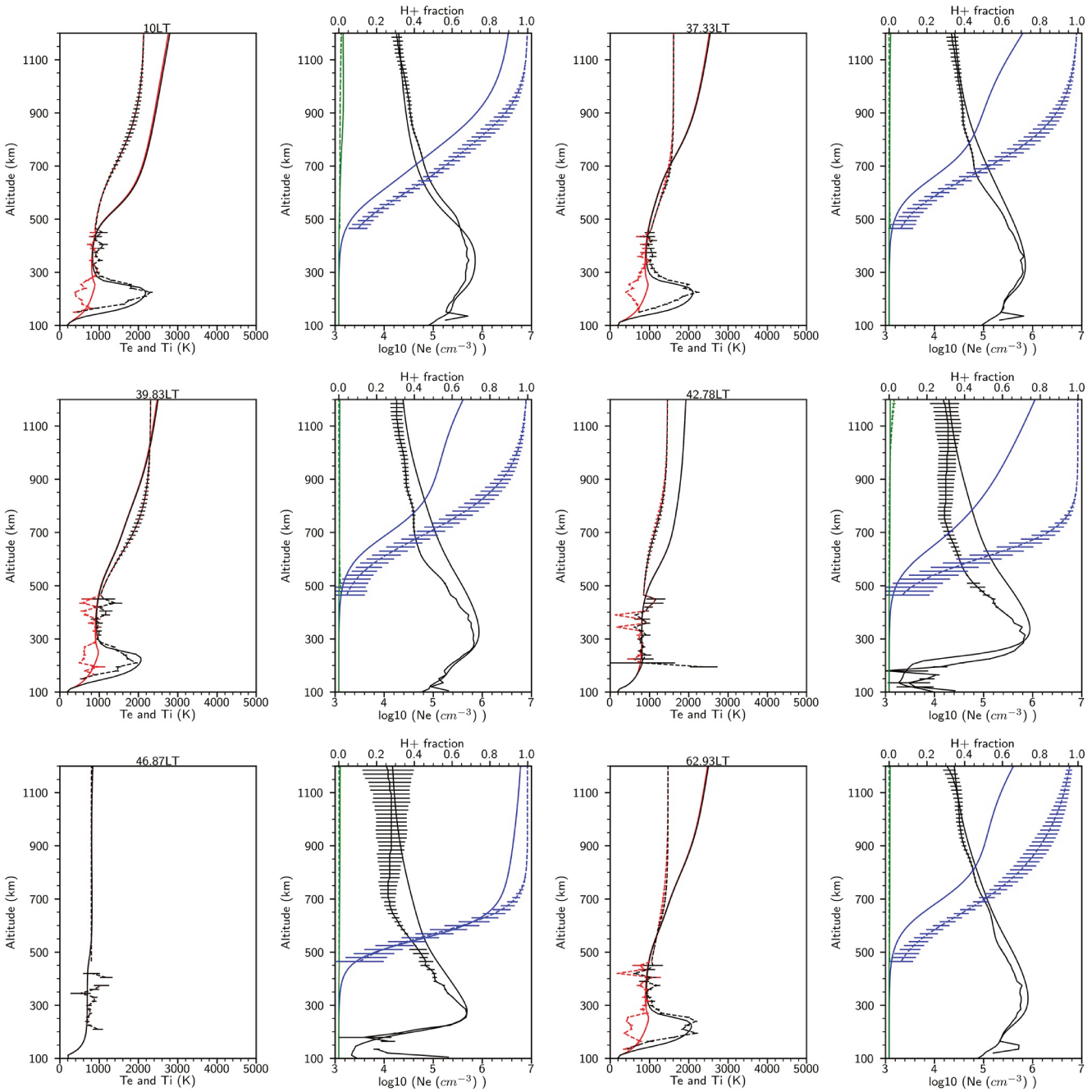

Figure 9. Measured and SAMI2-PE modeled parameter profile plots for six different times from September 1–4, 2020. Measured profiles include error bars. T_e and T_i are shown in black and red respectively on the same plots and N_e, H^+ fraction, and He^+ fraction are shown in black, blue, and green respectively on the same plots.

The heat flow was also found to be inversely proportional to the H^+ fraction and if we extend these conclusions to the topside, the diffusive thermal effect should be expected to induce the maximum heat flow at noon when concentrations of H^+ are at their lowest. The result of multiplying the H^+ heat flow by a factor of 10 shown in Figure 10, is an attempt to simulate the effect of large diffusive thermal contributions to the ion momentum equation. With the exception of increasing H^+ and electron temperatures in the topside very slightly (see Figure 10), no significant effects were noted. It is likely that the contribution of this term to the energy balance in the topside is overshadowed by the much larger electron heat flow.

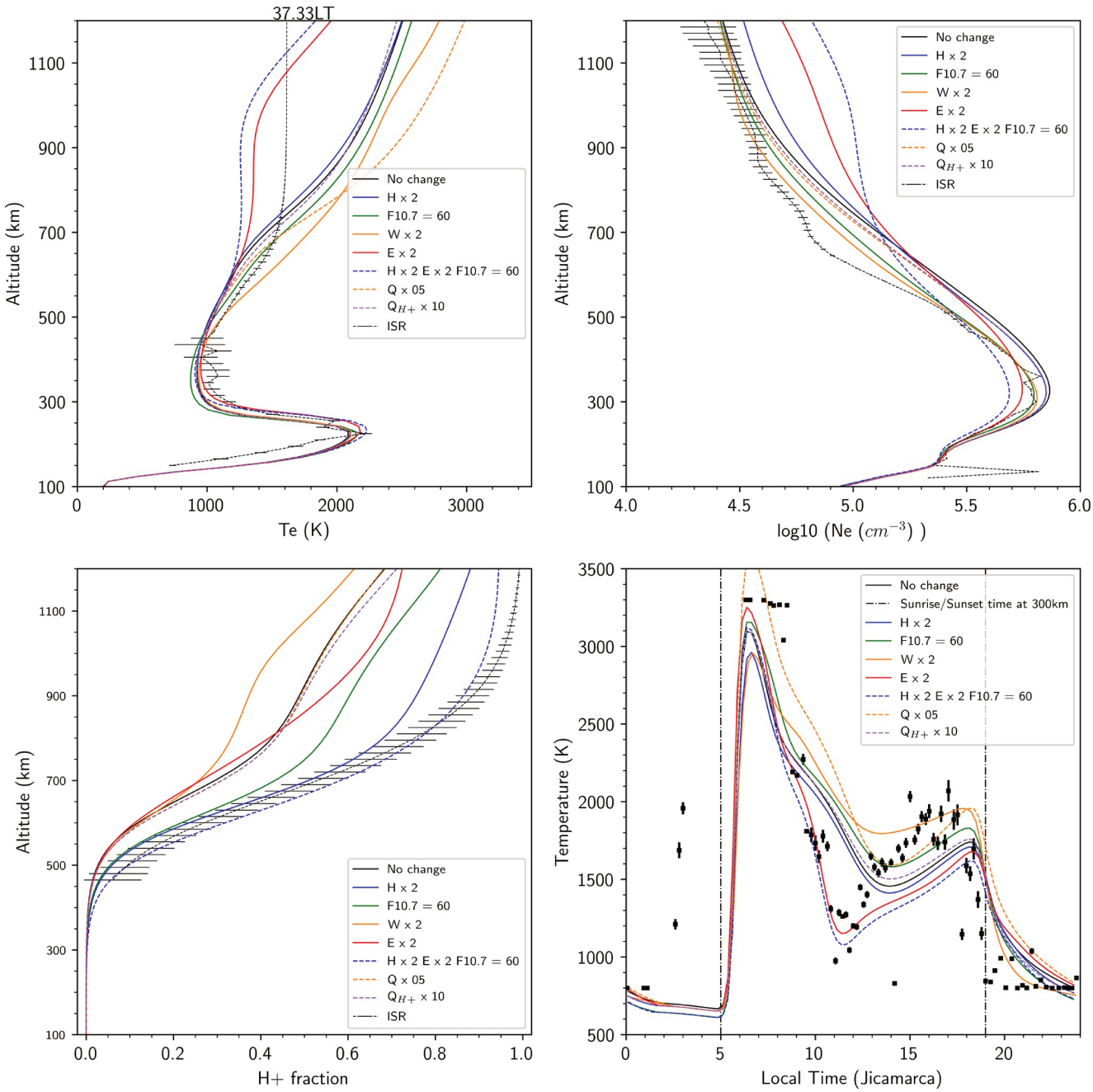

Figure 10. Sensitivity studies using modeled parameter profiles for 12:30LT on September 2, 2020. The effect of changes to neutral hydrogen, solar flux, neutral winds, electric field, and a combination of the above on T_i, N_e and H^+ was examined by comparing the modeled profiles to the measured ones shown in the same plots. The bottom right panel shows the effect of the same changes at a fixed altitude (700 km) over a 24 hr period on September 2, 2020. This altitude was chosen as the effect is more visible.

The thermoelectric term arises from a differential drift between electrons and ions along field lines leading to a current $J_{\parallel}$ (Schunk & Nagy, 2009). This term has the net effect of either increasing or decreasing the heat flow vector depending on the direction of the current. It can be calculated from the parallel current ($J_{\parallel}$) using the expressions in (St. Maurice Schunk, 1977; Conrad & Schunk, 1979; Schunk & Nagy, 2009). We do not have a satisfactory method of estimating this current in SAMI2-PE as it requires the knowledge of the field aligned thermal electron momentum which is unavailable in the model. The parallel current can alternatively be extracted from a global potential solver such as SAMI3, and inserted into SAMI2-PE to estimate the thermoelectric term.

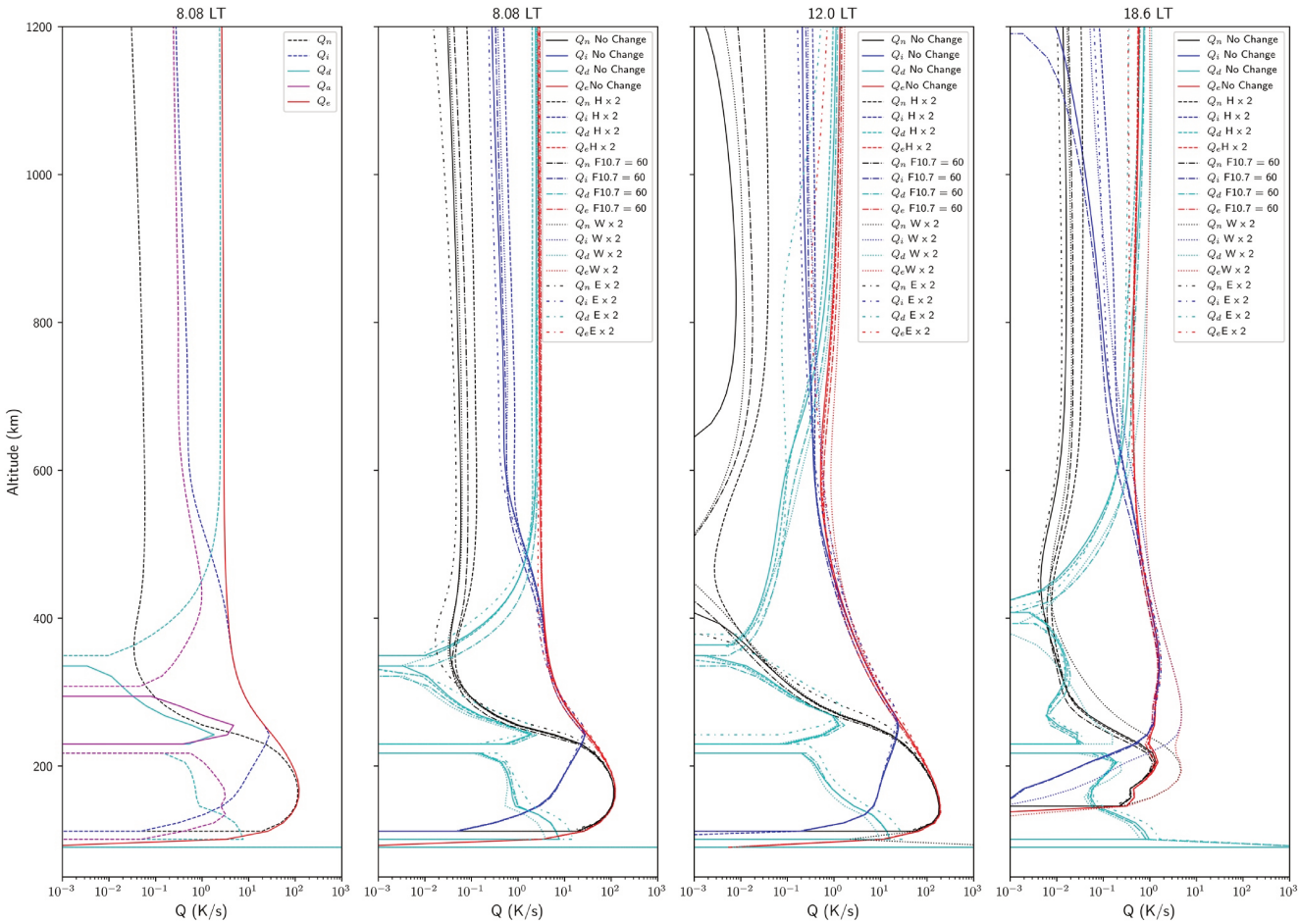

Figure 11. Heating/cooling rates are shown for 0800 LT on September 2, 2020 on the leftmost panel. Q_n denotes electron-neutral collisions, Q_i electron-ion collisions, Q_d heat conduction, Q_a transverse conduction and Q_e energetic electrons. Heating (cooling) rates are depicted using solid (dashed) lines. The next three panels show the changes that occur in the principal heating terms at three different times when the neutral hydrogen is doubled, solar flux decreased ($F_{10.7} = 60$), neutral winds doubled, electric field doubled, and a combination of the above. All curves are modeled using SAMI2-PE.

If the thermoelectric term were to change the total electron heat flow significantly, as illustrated in Figure 10, the effect on temperatures would be noticeable.

Thermal diffusion is yet another phenomenon not accounted for in the standard set of transport equations used by SAMI2 but included in higher moment equations. It arises from the effect that heat flow in any one of the species has on momentum balance (Schunk & Nagy, 2009). The authors in (Conrad & Schunk, 1979) have performed an extensive analysis of this effect and calculated different thermal diffusion coefficients which act together on the momentum equation to affect the relative drifts between species. If an O^+ and H^+ only atmosphere is assumed, and $T_{H+} = T_{O+}$, the figures in the study show that thermal diffusion and ordinary diffusion coefficients can be increased by large factors (up to threefold) proportionally to the relative temperature and/or ion fraction of the oxygen gas. When the H^+ fraction gets closer to unity however, the effect becomes less important. This implies that thermal diffusion effects are more significant at lower altitudes where O^+ is dominant, resulting in the heavier and cooler ions being driven upwards along field lines and lowering temperatures in the topside. The effect will be more pronounced at midday when the O^+ fraction is highest at all altitudes along field lines, and hints at the possible involvement of this mechanism in the significant temperature drops seen at midday in the data. Integrating it into the model could resolve the afternoon temperature discrepancies.

Further insight into the thermodynamic properties of the topside can be gained by examining the heating/cooling terms in the model, shown in the left panel of Figure 11. Heating (cooling) terms are drawn using solid (dashed) lines. Above 600 km, cooling is mediated primarily through thermal conduction along field lines and balances the

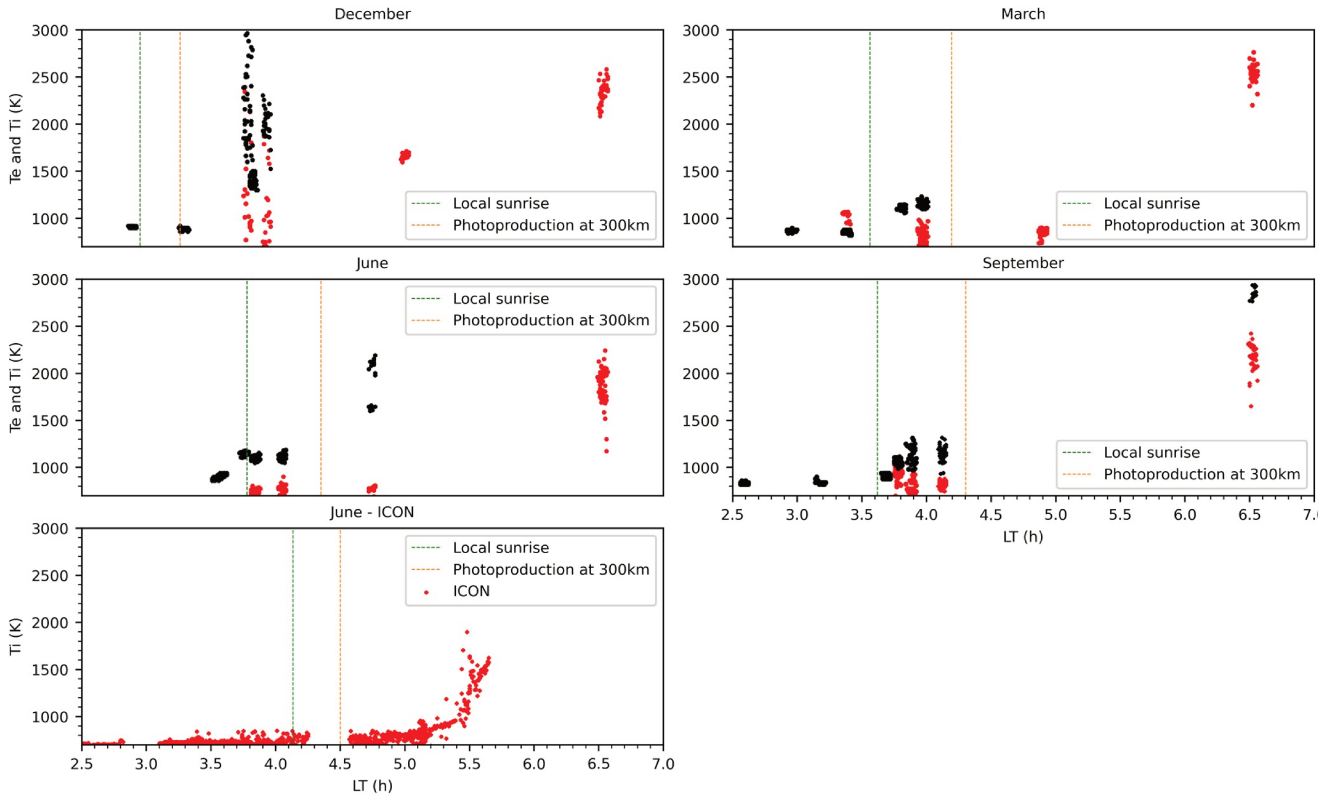

Figure 12. The uppermost four panels display DMSP T_e and T_i data compiled from March, June, September and December 2018–2020 at ≈850 km altitude. Satellite precession was used to sample slightly different local times in the predawn sector over Jicamarca. Conjunctions were counted whenever the satellite orbit crossed a cube centered at −11.95° ±5°,−76.87° ± 5° and 850 ± 15 km. The fifth panel shows ICON T_i statistics compiled from June, 2020, at ≈600 km altitude. Conjunctions were counted in the same manner but with an altitude window of 600 ± 15 km. In all the panels, the orange vertical dashed line indicates the earliest possible time of nonlocal photoelectron transport from the 300 km point on the field lines. The green dashed line indicates the time of local sunrise. Note that T_e shows a 400 K increase up to 1 hr before photoelectron transport onset.

heating caused by photoelectrons. The thermal conductivity coefficient is directly proportional to the temperature, the temperature gradient along field lines and the density, and inversely proportional to the collision frequency. The increased collision frequencies and decreased temperatures at lower altitudes result in this term becoming less significant. Below about 500 km, electron-ion collisions instead become the dominant cooling process.

The three remaining panels of Figure 11 display the sensitivity of the primary heating terms to changes in the model forcing parameters at three different local times. The most significant features appear in the mid-afternoon sector. These are:

- The cooling rate due to electron-neutral collisions is most strongly enhanced by an increase in neutral H. A decrease in the solar flux and an increase in neutral winds also contributes but to a lesser degree.
- Increasing the E field reduces the photoelectron heating rate and also electron-neutral collisional cooling, but the net effect is still a large decrease in noontime temperatures.

Returning to the topic of predawn heating observed in the September data, a similar phenomenon could be seen in satellite data. DMSP and ICON satellite statistics were gathered for T_e and T_i values from about 0300 LT to 0600 LT over a 10-day interval in the months of December, March, June, and September 2018–2020. These measurements are shown in Figure 12. An increase of roughly 400 K in T_e values can be seen in the first four panels at least 30 min earlier than the time at which non-local photoelectron transport begins (shown by dotted vertical orange lines) on the field lines crossing the spacecraft. In both the fall and summer plots, the electron temperatures began to increase around 0345 LT. Ion temperatures in contrast, do not increase until after 0500 LT which corresponds more closely to the sunrise times in the SAMI2/SAMI2-PE model. It is interesting to note that the increase of T_e occurs around the time of local sunrise (shown by green dotted lines) at the position of the

spacecraft. A slim possibility exists of it being due to spacecraft generated photoelectrons, but it is unlikely since the times do not match exactly.

The fifth panel of Figure 12 shows T_i values from the IVM instrument on board ICON for the month of June 2020. This month was chosen because it contained the fewest gaps in local time. The most notable feature in the ICON plot is the fact that the ion temperature only increases only after photoelectron transport begins, not before, as in the case of electron temperatures in the other panels. This constitutes a discrepancy with ISR data, which indicates an equal increase of both T_e and T_i around 0300 LT. Another discrepancy is in the onset time of predawn heating which is earlier in ISR data but which agrees with SWARM B data (Yang et al., 2020). Both of these require further study.

To test the implication of hydrogen and helium geocoronal emissions as well as interplanetary helium in predawn heating Lyman-α (121.6 nm), Lyman-β (102.6 nm), He I (58.4 nm), and He II (30.4 nm) fluxes were multiplied by a factor of 10 individually and together in SAMI2-PE, but very little effect was found in causing earlier sunrise times. This could indicate that although these wavelengths contribute to nighttime ionization, their magnitude in the predawn sector does not increase early enough to explain the appearance of predawn heating in the data.

One of the hypothesis advanced in (Hysell et al., 2015) to explain predawn heating was that of zonal transport of higher temperature plasma from the region of the terminator. The speed of the terminator at 300 km altitude is approximately 750 m/s. For zonal transport to account for increases in T_e values an hour before photoelectron transport on Jicamarca associated field lines, hotter plasma would need to migrate from tens of degrees to the east (where local times are an hour earlier) at higher speeds than the terminator, which is unlikely given the lower speeds of zonal drifts. Furthermore, a simulation was run using SAMI3 (which includes zonal transport) with a grid resolution of 2° and no evidence was found of significantly earlier predawn heating than what is seen in SAMI2.

The effect of including zonal thermal conduction terms in the model is also unlikely to produce earlier predawn heating in the model, since their influence on the magnitude of the heat flow in the energy equation in the ionosphere is in general not significant. An expression is given in (Rees, 1989) in which the thermal conductivity is described as a tensor with components in both the longitudinal and zonal directions. The horizontal and transverse components of the conductivity are very small in comparison to the parallel component, owing to the much larger value of the gyrofrequency in comparison to the collision frequency at the altitudes studied. In the region of the terminator, the zonal temperature gradient may possibly be large enough to overcome the small value of the zonal conductivity, effectively contributing to the magnitude of the heat flow. However, the influence of this effect would be on the plasma surrounding the terminator, still thousands of kilometers away from the region of observation. On a different note, this effect should still be examined to see if it has an impact on increasing local electron temperatures at sunrise.

In view of the above analysis, a more plausible hypothesis for predawn heating could be that airglow, as mentioned at the beginning of the manuscript, or scattered sunlight from the terminator could be initiating photoproduction at the base of the field lines passing through Jicamarca.

An additional possibility worth investigating is that predawn heating, instead of being generated by photoelectron transport, could be the result of field aligned thermal electron currents giving rise to Ohmic heating in the predawn sector. Hemispheric asymmetries in neutral winds or conductivities near the terminator could give rise to large field aligned currents. An estimate of $J_{\parallel}$ would be needed from a potential solver as mentioned earlier to test this hypothesis.

5. Summary and Conclusions

This study presented the most recent ISR measurements of the equatorial topside ionosphere at extremely low solar flux. The measurements were made using Jicamarca's long pulse/double pulse Faraday mode with an integration time of approximately 11 min, and for three different months during the 2019–2020 solar minimum with solar flux levels ranging from 66 to 71.

The salient features of the measurements include a strong day-to-day variability of densities and the O^+/H^+ transition height, earlier occurrence of predawn heating than previous studies, and the presence of negligible fractions of He^+ at all altitudes.

SAMI2-PE recovers many of the features present in the data but the discrepancy with measurements is far more pronounced than in the previous topside study at more moderate solar flux (Hysell et al., 2015). Some of these discrepancies include lower concentrations of H^+ at high altitudes in the model, inability to simulate the large temperature decrease at noon present in the data, gradual decreases in the temperature at dawn rather than the sudden drop seen post-sunset in the data, and the absence of predawn heating in the model. In addition, a sensitivity analysis was carried out to analyze the effect of various forcing agents on the output of the model and to gain a better understanding on required revisions. Insight into the thermodynamic processes involved in the composition, dynamics, and energetics of the topside was arrived at by examining the effect of the same forcing agents on the heating terms in the energy equation.

Some revisions are proposed to the model which include:

1. Estimation of the parallel current $J_{\parallel}$ and thus the thermoelectric term using global potential solvers such as SAMI3 and examination of its effect on temperatures. Inclusion of Ohmic heating in the model using $J_{\parallel}$ and evaluation of its effect on predawn heating.
2. Addition of thermal diffusion to the ion and electron momentum equations in SAMI2 to better reproduce midday temperature decreases.
3. Obtaining better estimates of the neutral H densities used to initialize the model. The ongoing work by Waldrop et al. (2006) on this topic should be consulted.
4. Comparing HWM14 neutral wind estimates to upcoming ICON and Jicamarca neutral wind data and inserting an improved wind model into SAMI2.
5. Obtaining electric field estimates from satellite data and using them to develop campaign specific $E \times B$ drift models (see for example (Huba et al., 2017)).
6. Investigating the effect of airglow on photoproduction and including relevant routine into the model to simulate predawn heating.
7. Performing a sensitivity analysis on the effect of including zonal electron thermal conductivity terms in the enhancement of sunrise temperatures.
8. Reexamining the Chapman grazing incidence function (Varney, 2012) to evaluate its possible limiting effect on earlier sunrise times

Furthermore, a few improvements to the full-profile analysis can be made which consist in adding more elaborate noise power bias correction as described in Appendix A, improving Faraday rotation and double pulse estimates at sunrise times, and including the ability to measure accurate nighttime temperatures which at the moment are set by a lower ceiling of 800 K. It would be insightful to compare electron temperatures from the IVM instrument on board the COSMIC-2/FORMOSAT-7 which has noon passes with Jicamarca and scheduled for operational release in June 2021, with those obtained in this manuscript.

Appendix A: Correcting Noise Estimates

The purpose of this Appendix is to present a simple formula for correcting noise power estimates used in the full-profile algorithm. As described in the Methods section of this paper, an order statistics based clutter removal technique is applied to receiver voltage samples in the Jicamarca hybrid long pulse/double pulse Faraday experiment. This technique however, introduces an error in the estimate of the true expectation due to the skewness of the underlying distribution. Unlike receiver voltage samples that follow Gaussian statistics and are symmetrical about the mean, power samples (noise or signal) follow a Gamma distribution with a skewness dependant upon the number of degrees of freedom. Lag products other than zero follow a non-central generalized Laplacian distribution (NGL; Mathai, 1993) with a skewness not only dependant upon the number of degrees of freedom but on the correlation between each of the terms in the product. The NGL distribution tends toward a Gamma distribution when the correlation between samples is high (such as in lag zero or noise power samples), and toward a symmetrical Laplacian distribution when the correlation is low such as in lag products with long time delays.

The current Appendix pertains to noise samples which follow pure Gamma distributions, but can also be applied to signal power or lag zero distributions. Bias corrections for lags greater than zero will be described in Appendix B.

In the paragraphs below, the necessary theoretical derivations will be presented followed by an overview of the numerical methods employed. We will then conclude with a specific bias correction formula that can be integrated into the full-profile algorithm but can be adapted to other programs that process data contaminated by clutter.

A1. Nature of Noise Distribution

The voltage samples collected from the radar receivers at Jicamarca are a superposition of two distributions: a correlated multivariate normal distribution which contains information about the ionosphere and an uncorrelated multivariate Gaussian distribution corresponding to various sources of noise (electronic, thermal, and sky noise). It is not possible to extract the noise from the signal in real time however the mean noise power can be approximated by taking the average of samples during the "Transmitter Off" periods in between pulse transmissions where there is no signal contribution. This practice is based on the assumption that the noise does not vary rapidly enough to fluctuate considerably within the integration time of the experiment.

As described in the previous section, noise power samples follow a pure Gamma distribution. Since the noise power is calculated by summing the squares of the real and imaginary components of the noise voltage samples (in phase and quadrature components) where each one has a degree of freedom of $k = \frac{1}{2}$, it possesses a degree of freedom of $k = 1$.

To reduce the skewness of the distribution (given by $\frac{2}{\sqrt{k}}$), N power samples can be added together which results in a distribution with N degrees of freedom ($k = \mathrm{N}$). Longer integration times always lead to less skewness as larger number of samples are added, but the integration time is limited by the physics of the experiment and the behavior of clutter or artifacts.

In the current study, sixteen sums comprised of 22 noise samples each are sorted in ascending order and clutter removal is performed as per the technique mentioned in the Methods section.

A2. Deriving the Noise Power Distribution

After applying the clutter removal technique based on order statistics, and removing a fixed number of samples from both sides of our ordered list, a reduced sample set is obtained that can no longer be regarded as gamma distributed. The degree to which the mean of this reduced sample set deviates from the true expectation of the underlying distribution depends on the skewness and the number of samples retained.

However, a generic formula can be developed that can correct the bias in the sample mean of the reduced sample set. Before delving into the details of the derivation, a proof will be provided of the statistical assumptions advanced in the previous paragraphs.

Let us say we have two normally distributed random variables, with zero mean, given by $X \sim \mathcal{N}(0, \sigma_x^2)$, and $Y \sim \mathcal{N}(0, \sigma_y^2)$, which in this paper's context correspond to the real and imaginary parts of the in-phase and quadrature elements of our receiver samples. In this experiment, $\mu_x = \mu_y = 0$, and $\sigma_x^2 = \sigma_y^2$. Therefore, the subscript free notation σ will be used. To calculate the noise power, each of these variables is squared, giving rise to two i.i.d. gamma distributions with the following properties:

$$X^2, Y^2 \sim \Gamma(k = \frac{1}{2}, \theta = 2\sigma^2)$$

where θ represents the scale factor, and k is the number of degrees of freedom.

The derivation of a Gamma distribution $Z \sim \Gamma(k, \theta)$ from any normal distribution, let us say $X \sim \mathcal{N}(0, \sigma^2)$, can be accomplished as follows:

$$
\begin{aligned}
P(X^2 < z) &= P(|X| < \sqrt{z}) \\
&= P(-\sqrt{z} < X < \sqrt{z}) \int_{-\sqrt{-z}}^{\sqrt{z}} f_X(x) \text{ where } f_X(x) = \frac{1}{\sqrt{2\pi\sigma^2}} e^{-\frac{(x-\mu)^2}{2\sigma^2}} \\
&= \int_{-\infty}^{\sqrt{z}} f_X(x) - \int_{-\infty}^{-\sqrt{z}} f_X(x) \\
&= F_X(\sqrt{z}) - (1 - F_X(\sqrt{z})) \\
&= 2F_X(\sqrt{z}) - 1
\end{aligned}
$$

$$
\begin{aligned}
f_X(x) &= \frac{d}{dz}(2F_X(\sqrt{z}) - 1) \\
&= 2\frac{d}{dz}\left(\frac{1}{2}\left(1 + erf\left(\frac{\sqrt{z}-\mu}{\sigma\sqrt{2}}\right)\right)\right) \\
&= \frac{2}{\sqrt{\pi}} e^{-\frac{z}{2\sigma^2}} \left(\frac{1}{\sqrt{2}\sigma}\right)\left(-\frac{1}{2\sqrt{z}}\right) \\
&= \frac{1}{\sqrt{\pi}\sqrt{2}\sigma} e^{-\frac{z}{\theta}} z^{\frac{1}{2}} \\
&= \frac{1}{\Gamma\left(\frac{1}{2}\right)\theta^{\frac{1}{2}}} e^{-\frac{z}{\theta}} z^{\frac{1}{2}}, \quad \text{where } \theta = 2\sigma^2,\ k = \frac{1}{2}
\end{aligned}
$$

The factor $\sqrt{\pi}$ is replaced by $\Gamma(\frac{1}{2}n) = \frac{(n-2)!\sqrt{\pi}}{2^{(n-1)/2}}$ with $n = 1$.

From the derivation above, it can be concluded that the distribution obtained from the square of a normal random variable with zero mean, and variance equal to σ^2 is a gamma distribution with $k = \frac{1}{2}$ degrees of freedom and a scale factor of $2\sigma^2$ (Note also that this is a limiting case of the NGL distribution described earlier in which the correlation is taken to be unity, since we are squaring a single sample).

When two gamma distributed random variables, X and Y, possessing the same scale factor (θ) but different degrees of freedom (k_1 and k_2) are added together, the following can be posited: $X + Y \sim \Gamma(k_1 + k_2, \theta)$. This expression can be derived by convolving the PDFs of each of the individual gamma random variables. This principle only applies if they are statistically independent, as is the case with the noise power. This theorem, therefore does not hold true in the case of correlated variables such as lag products.

Here is a proof that the sum of two or more gamma distributions is another gamma distribution:

$$
\begin{aligned}
f_{X+Y}(z) &= \int_0^z \frac{1}{\Gamma(k_1)\theta^{k_1}} e^{-\frac{x}{\theta}} x^{k_1-1} \frac{1}{\Gamma(k_2)\theta^{k_2}} e^{-\frac{(z-x)}{\theta}} (z-x)^{k_2-1} dx \\
&= \frac{1}{\theta^{k_1}} \frac{1}{\theta^{k_2}} e^{-\frac{z}{\theta}} \int_0^z \frac{x^{k_1-1}(z-x)^{k_2-1}}{\Gamma(k_1)\Gamma(k_2)} dx \\
&= \frac{1}{\theta^{k_1+k_2}} e^{-\frac{z}{\theta}} z^{k_2-1} z^{k_1-1} \int_0^1 \frac{t^{k_1-1}(1-t)^{k_2-1}}{\Gamma(k_1)\Gamma(k_2)} dt, \text{where } x = zt \\
&= \frac{e^{-\frac{z}{\theta}} z^{k_2+k_1-1}}{\theta^{k_1+k_2}\Gamma(k_1+k_2)}
\end{aligned}
$$

The last step was arrived at by noticing that the integral of the numerator is the same as the integral of a β PDF (in this case equal to 1) multiplied by the function $\beta(k_1, k_2) = \frac{\Gamma(k_1)\Gamma(k_2)}{\Gamma(k_1+k_2)}$.

A3. Estimating the True Expectation From the Biased Sample Mean

To derive an expression for calculating the true expectation from the sample mean, we first present a closed-form expression that approximates the sample mean as a function of the percentage of samples removed. Using this expression and exponential fitting, bias correction formulas are presented that depend only on the degrees of freedom (k). These correction formulas can be applied not only in the context of this study, but to any sample-set to which clutter removal is applied, provided it is gamma-distributed.

One should note that the operation of removing an equal number of samples from each side of the discrete ordered sample set, is analogous to discarding areas of equal probability from both ends of the continuous underlying probability density function. This is due to the frequentist nature of the experiment whereby the number of outcomes contained in a subset of the sample space is proportional to the probability, $P(x) \approx \frac{n_x}{n_t}$, where n_x is the number of trials where the event x occurred, and n_t is the total number of trials.

Since the expectation of a random variable X is given by $\mu = \int xf(x)dx$, the first step in obtaining an expression for the sample mean of the "chopped" list is to evaluate the integral below in between the areas of the distribution function that we wish to discard:

$$
\begin{aligned}
g(a,\ b) &= \int_a^b x \frac{e^{-\frac{x}{\theta}} x^{k-1}}{\Gamma(k)\theta^k} dx \\
&= \frac{\Gamma(k')\theta^{k'}}{\Gamma(k)\theta^k} \int_0^b \frac{e^{-\frac{x}{\theta}} x^{k'-1}}{\Gamma(k')\theta^{k'}} dx - \frac{\Gamma(k')\theta^{k'}}{\Gamma(k)\theta^k} \int_0^a \frac{e^{-\frac{x}{\theta}} x^{k'-1}}{\Gamma(k')\theta^{k'}} dx \ \text{ where } \ k' = k+1 \\
&= \frac{\Gamma(k')\theta^{k'}}{\Gamma(k)\theta^k} [F(b; k+1, \theta) - F(a; k+1, \theta)]
\end{aligned}
$$

On the last line, $F(x; k, \theta) = \frac{\gamma(k,\ \theta/x)}{\Gamma(k)}$ is the CDF of the gamma distribution. The next step is to transform the function $g(a, b)$ into an estimate of the sample mean by normalizing it to the probability of the area that was retained, which is the difference in the values of the CDF between a and b. This is because the probability space of the chopped distribution no longer extends from $-\infty$ to $+\infty$, but is located only between a and b.

The sample mean can therefore be estimated by:

$$
\overline{X}_{est}(a, b) = \frac{\Gamma(k')\theta}{\Gamma(k)} \frac{[F(b; k+1, \theta) - F(a; k+1, \theta)]}{[F(b; k, \theta) - F(a; k, \theta)]} \tag{A1}
$$

A correction factor can be determined by dividing the true expectation by the estimate above: $\frac{k\theta}{\overline{X}_{est}(a,\ b)}$. The dependency of the expression on the scale factor is negligible for $k > 10$ and depends only on a, b, and k. Note that the total probability of the areas to the left of a and to the right of b are equal and can be denoted as p. Several curves of the correction factor were plotted versus p for different values of k. Exponential fitting was performed for intervals of k relevant to this study and the following generic coefficients were found:

k = 10–50: 0 cm

$$
\begin{aligned}
A &= -0.06304944\exp\ (-0.09477955k) - 0.00624749 \\
B &= 6.02 \\
C &= 0.07159175\exp\ (-0.09402204k) + 0.00717884
\end{aligned}
$$

k = 50–100:

$$
\begin{aligned}
A &= -0.01645125\exp\ (-0.02820797k) - 0.00209797 \\
B &= 6.06 \\
C &= 0.01895456\exp\ (-0.02817038k) + 0.00242496
\end{aligned}
$$

$k = 100$–150:

$$A = -0.0093211\exp\ (-0.01631k) - 0.001232$$
$$B = 6.07$$
$$C = 0.01075326\exp\ (-0.01629058k) + 0.00142467$$

The correction factor can be determined by plugging the above coefficients into the expression: $A\exp(-Bp) + C + 1$. In order to include bias correction given by the above expression into the full-profile algorithm, the following steps are needed:

1. Determine the number of degrees of freedom. Since both in phase and quadrature elements are added, for N integrations (or sample summations), $k = N$.
2. Determine the correction factor based on the formulas presented above and the value of p. For example, if six samples are rejected out of a set of 16, the value of $p = \frac{3}{16}$.
3. Calculate the sample mean from the reduced data set which was subjected to the clutter removal technique. Multiply the sample mean by the correction factor to yield an unbiased estimate of the true expectation.

Appendix B: Correcting Lag Product Estimates

To recover an error correction formula for lag products, a similar procedure can be followed to the one in Appendix A. The bias in lag products that results from the decluttering technique is less significant than in the case of noise power samples because of less skewness in the underlying distribution. The smaller skewness is due to the fact that for lags other than zero, the correlation is less than unity and the NGL distribution becomes more symmetric, and to the fact that a greater number of samples (128) are averaged. Nevertheless, we will discuss the theory of the lag product bias correction in the following paragraphs.

Just as with noise samples, backscatter measurements are stochastic in nature but unlike them, they are correlated and thus give rise to lag products that follow the more complex NGL distribution described in Appendix A. The only exception is for lag zero which similarly to noise power samples, follows a pure Gamma distribution.

If the lag product of two samples is denoted by XY^* (where Y^* is the complex conjugate of Y), it can be decomposed into four components: $\Re(X)\Re(Y) + i\Re(X)\Im(Y) + i\Re(X)\Im(Y) + \Im(X)\Im(Y)$, each following its own probability density function. The correlation between the real and imaginary parts of both samples (in phase and quadrature elements), is negligible resulting in the formation of a symmetrical Laplace distribution with zero expectation (see expression for $g(z_{tot})$, setting $\rho = 0$). Because of its symmetry, this term does not require bias correction. Thus only the real part of the lag product, which includes the first and last terms in the sum, requires bias correction. It can be noted that the product between two correlated normal random variables X and Y can be written in the form of a difference between two uncorrelated gamma distributed random variables: $Z = \frac{1}{4}(X+Y)^2 - \frac{1}{4}(X-Y)^2$. The terms in parenthesis follow normal distributions: $X - Y \sim \mathcal{N}(0, 2\sigma^2(1-\rho))$ and $X + Y \sim \mathcal{N}(0, 2\sigma^2(1+\rho))$,where ρ is the correlation coefficient, which depends on the lag and range. Consequently, each of the two terms that comprise Z follow distinct Gamma distributions given by:

$$\frac{1}{4}(X+Y)^2 \sim \Gamma(k=1,\ \ \theta = \frac{4}{4}\sigma^2(1+\rho)) = \Gamma(k=1,\ \ \theta = \sigma^2(1+\rho))$$

$$\frac{1}{4}(X-Y)^2 \sim \Gamma(k=1,\ \ \theta = \frac{4}{4}\sigma^2(1-\rho)) = \Gamma(k=1,\ \ \theta = \sigma^2(1-\rho))$$

when lag products are integrated over several pulse returns, it is easier to derive the distribution of $Z_{tot} = (Z_1 + Z_2 + .. + Z_n)/n$ by summing its individual components first and taking the difference after. This gives us $Z_{tot} = \frac{1}{4}(X+Y)^2 - \frac{1}{4}(X-Y)^2$ just as previously, however with n degrees of freedom. Z_{tot} can then be written as:

$$\frac{1}{4}(X+Y)^2 \sim \Gamma(k=n,\ \ \theta_1 = \sigma^2(1+\rho))$$

$$\frac{1}{4}(X-Y)^2 \sim \Gamma(k=n,\ \ \theta_2 = \sigma^2(1-\rho))$$

The final step in deriving the PDF of Z_{tot} is to employ the expression given by (Mathai, 1993) describing the difference between two gamma distributed random variables:

$$g(z) = \begin{cases} c_1 z^{(k_1+k_2)/2-1} e^{-z/2(1/\theta_1-1/\theta_2)} W_{(k_1-k_2)/2,(1-k_1-k_2)/2}(\theta_0 z) & z > 0 \\ c_2(-z)^{(k_1+k_2)/2-1} e^{-z/2(1/\theta_1-1/\theta_2)} W_{(k_1-k_2)/2,(1-k_1-k_2)/2}(-\theta_0 z) & z \le 0 \end{cases}$$

where $c = c_1 = c_2 = 1/(\Gamma(k)(\theta_1+\theta_2)^k)$, and W is the Whittakker function, equivalent to $W_{0,\mu}(z) = \sqrt{\frac{z}{\pi}} K_\mu(\frac{z}{2})$.

Using the same procedure as in Appendix A, we first derive a theoretical estimate of our sample mean given by:

$$\overline{X}_{est}(a,b) = \frac{g(b;k,\theta,\rho) - g(a;k,\theta,\rho)}{G(b;k,\theta,\rho) - G(a;k,\theta,\rho)} \tag{B1}$$

where g is the PDF and G is the corresponding CDF of the lag product distribution (determined by numerical quadrature). The bias correction factor can be found by dividing the true expectation by the sample mean estimate. The remaining steps can be reproduced by the reader using the same procedure employed for noise power bias correction. A summary of these steps are:

1. Obtain the value of k and p that will be used in the experiment
2. Generate curves of the correction factor versus the correlation coefficient ρ
3. Perform exponential fitting of the curves to obtain a generic expression to be used for the entire algorithm
4. For each measured lag product, determine the correlation coefficient between the real parts of the samples
5. Calculate the correction factor for the lag product sample using the generic expression above, and multiply the biased sample mean by the correction factor to obtain an estimate of the true expectation.

Data Availability Statement

Data used for this publication are available through the Madrigal database (see http://www.openmadrigal.org.), and found under Jicamarca ISR experiments. The DMSP data used in this study can be obtained at the following link: http://cedar.openmadrigal.org/. ICON is supported by NASA's Explorers Program through contracts NNG-12FA45 C and NNG12FA42I. ICON data are processed in the ICON Science Data Center at UCB and available at: https://icon.ssl.berkeley.edu/Data.

Acknowledgments
The Jicamarca Radio Observatory is a facility of the Instituto Geofisíco del Perú operated with support from NSF award AGS-1732209 through Cornell. The help of the staff is much appreciated. We would like to acknowledge Dr. Marc Hairston with providing additional data and answering all queries related to DMSP datasets. We would like to thank Dr. Joe Huba for helpful discussions on SAMI2.

References

Akiba, T., Sano, S., Yanase, T., Ohta, T., & Koyama, M. (2019). *Optuna: A next-generation hyperparameter optimization framework*.

Alken, P., Thebault, E., Beggan, C. D., Amit, H., Baerenzung, J., Bondar, J., et al. (2021). International geomagnetic reference field: The thirteenth generation. *Earth Planets and Space*, *73*(1), 49. https://doi.org/10.1186/s40623-020-01288-x

Aponte, N., Brum, C. G., Sulzer, M. P., & González, S. A. (2013). Measurements of the O+ to H+ transition height and ion temperatures in the lower topside ionosphere over Arecibo for equinox conditions during the 2008-2009 extreme solar minimum. *Journal of Geophysical Research: Space Physics*, *118*(7), 4465–4470. https://doi.org/10.1002/jgra.50416

Baker, K. B., & Wing, S. (1989). A new magnetic coordinate system for conjugate studies at high latitudes. *Journal of Geophysical Research*, *94*(A7), 9139. https://doi.org/10.1029/JA094iA07p09139

Balsley, B. B. (1964). Evidence of a stratified echoing region at 150 kilometers in the vicinity of the magnetic equator during daylight hours. *Journal of Geophysical Research*, *69*, 1925–1930.

Banks, P. M., Schunk, R. W., & Raitt, W. J. (1976). *The topside ionosphere a region of dynamic transition!*. Retrieved from www.annualreviews.org

Bhavnani, K. H., & Hein, C. A. (1994). *An improved algorithm for computing altitude dependent corrected geomagnetic coordinates*. Phillips Laboratory, Geophysics Directorate, Hanscom Air Force Base. PL-TR-94-2310.

Brinton, H. C., Mayr, H. G., & Potter, W. E. (1975). Winter bulge and diurnal variations in hydrogen inferred from AE-C composition measurements. *Geophysical Research Letters*, *2*(9), 389–392. https://doi.org/10.1029/GL002i009p00389

Carlson, H. C. (1966). Ionospheric heating by magnetic conjugate-point photoelectrons. *Journal of Geophysical Research*, *71*(1), 195–199. Retrieved from http://doi.wiley.com/10.1029/JZ071i001p00195

Carlson, H. C. (1968). Most Recent Studies of Low Latitude Effects Due to Conjugate Location Heating. *Radio Science*, *3*(7), 668–673. Retrieved from http://doi.wiley.com/10.1002/rds196837668

Chakrabarti, S. (1984). EUV (800-1400) observations of the tropical airglow. *Geophysical Research Letters*.

Chamberlin, P. C., Woods, T. N., & Eparvier, F. G. (2008). Flare Irradiance Spectral Model (FISM): Flare component algorithms and results. *Space Weather*, *6*(5). https://doi.org/10.1002/rds196837668

Chau, J. L., & Kudeki, E. (2006). Statistics of 150-km echoes over Jicamarca based on low-power VHF observations. *Annals of Geophysics*, *24*(5), 1305–1310.

Conrad, J. R., & Schunk, R. W. (1979). Diffusion and heat flow equations with allowance for large temperature differences between interacting species. *Journal of Geophysical Research: Space Physics*, *84*(A3), 811–822. https://doi.org/10.1029/ja084ia03p00811

Drob, D. P., Emmert, J. T., Meriwether, J. W., Makela, J. J., Doornbos, E., Conde, M., et al. (2015). An update to the horizontal wind model (hwm): The quiet time thermosphere. *Earth and Space Science*, *2*, 301–319. https://doi.org/10.1002/2014EA000089

Farley, D., Balsley, B. B., Woodman, R., & McClure, J. (1970). Equatorial spread F: Implications of VHF radar observations. *Journal of Geophysical Research*.

Farley, D. T. (1969). Faraday rotation measurements using incoherent scatter. *Radio Science*, *4*(2), 143–152. https://doi.org/10.5194/angeo-24-1305-2006

Farley, D. T., McClure, J. P., Sterling, D. L., & Green, J. L. (1967). Temperature and composition of the equatorial ionosphere. *Journal of Geophysical Research*, *72*(23), 5837–5851. https://doi.org/10.1029/ja075i034p07199

Forbes, J. (1981). The equatorial electrojet. *Reviews of Geophysics*, *19*, 469.

Heelis, R. A., Coley, W. R., Burrell, A. G., Hairston, M. R., Earle, G. D., Perdue, M. D., & Lippincott, C. R. (2009). Behavior of the O+/H+ transition height during the extreme solar minimum of 2008. *Geophysical Research Letters*, *36*(18). https://doi.org/10.1029/2009GL038652

Hein, C. A., & Bhavnani, K. H. (1996). *An expanded altitude algorithm for computing altitude-dependent corrected geomagnetic coordinates*. Phillips Laboratory, Geophysics Directorate, Hanscom Air Force Base. PL-TR-96-2274.

Heres, W., & Bonito, N. A. (2007). *An alternative method of computing altitude adjustment [sic] corrected geomagnetic coordinates as applied to IGRF Epoch 2005*. Phillips Laboratory, Geophysics Directorate, Hanscom Air Force Base. HA-TR-2007-1190.

Holt, J. M., Rhoda, D. A., Tetenbaum, D., & Eyken, A. P. V. (1992). Optimal analysis of incoherent scatter radar data. *Radio Science*, *27*(3), 435–447.

Høymork, S., Pécseli, H. L., Lybekk, B., Trulsen, J., & Eriksson, A. (2000). The equatorial electrojet. *Journal of Geophysical Research*, *105*(A8), 18519–18535.

Huba, J. D., Joyce, G., & Feder, J. A. (2000). Sami2 is another model of the ionosphere (SAMI2): A new low-latitude ionosphere model. *Journal of Atmospheric and Terrestrial Physics*, *105*(A10), 23035–23053.

Huba, J. D., Maute, A., & Crowley, G. (2017). SAMI3 ICON: Model of the ionosphere/plasmasphere system. *Space Science Reviews*, *212*(1–2), 731–742. https://doi.org/10.21236/ada324654

Hysell, D. L. (2000). Incoherent scatter experiments at Jicamarca using alternating codes. *Radio Science*, *35*(6), 1425–1435. https://doi.org/10.1029/91rs02922

Hysell, D. L., Chau, J. L., & Huba, J. D. (2009). Topside measurements at Jicamarca during solar minimum. *Annals of Geophysics*, *27*, 427–439.

Hysell, D. L., Milla, M. A., Rodrigues, F. S., Varney, R. H., & Huba, J. D. (2015). Topside equatorial ionospheric density, temperature, and composition under equinox, low solar flux conditions. *Journal of Geophysical Research: Space Physics*, *120*(5), 3899–3912. https://doi.org/10.1002/2015JA021168

Hysell, D. L., Milla, M. A., & Woodman, R. F. (2017). High-altitude incoherent-scatter measurements at Jicamarca. *Journal of Geophysical Research: Space Physics*, *122*(2), 2292–2299. https://doi.org/10.1002/2016JA023569

Hysell, D. L., Vierinen, J., & Sultzer, M. P. (2019). The case for combining a large low-band very high frequency transmitter with multiple receiving arrays for geospace research: A geospace radar. *Radio Science*, *54*(7), 533–551.

Kakinami, Y., Balan, N., Liu, J. Y., & Oyama, K. I. (2010). Predawn ionospheric heating observed by Hinotori satellite. *Journal of Geophysical Research: Space Physics*, *115*(1). https://doi.org/10.1029/2009JA014334

Klenzing, J., Simões, F., Ivanov, S., Heelis, R. A., Bilitza, D., Pfaff, R., & Rowland, D. (2011). Topside equatorial ionospheric density and composition during and after extreme solar minimum. *Journal of Geophysical Research: Space Physics*, *116*(12). https://doi.org/10.5194/angeo-27-427-2009

Kockarts, G. (2002). Aeronomy, a 20th century emergent science: The role of solar Lyman series. *Annals of Geophysics*, *20*(5), 585–598. https://doi.org/10.5194/angeo-20-585-2002

Lehtinen, M. S., & Huuskonen, A. (1996). General incoherent scatter analysis and GUISDAP. *Journal of Atmospheric and Terrestrial Physics*, *58*(1–4), 435–452. https://doi.org/10.1016/0021-9169(95)00047-X

Lehtinen, M. S., Huuskonen, A., & Pirttilä, J. (1996). First experiences of full-profile analysis with GUISDAP. *Annals of Geophysics*, *14*(12), 1487–1495. Retrieved from https://angeo.copernicus.org/articles/14/1487/1996/

Levenberg, K. (1944). A method for the solution of certain non-linear problems in least squares. *Quarterly of Applied Mathematics*, *2*, 164–168.

MacPherson, B., González, S. A., Bailey, G. J., Moffett, R. J., & Sulzer, M. P. (1998). The effects of meridional neutral winds on the O + −H + transition altitude over Arecibo. *Journal of Geophysical Research: Space Physics*, *103*(A12), 29183–29198. https://doi.org/10.1029/98JA02660

Marquardt, D. W. (1963). An algorithm for least-squares estimation of nonlinear parameters. *Journal of the Society for Industrial and Applied Mathematics*, *11*(2), 431–441. https://doi.org/10.1137/0111030

Mathai, A. (1993). On noncentral generalized laplacianness of quadratic forms in normal variables. *Journal of Multivariate Analysis*, *45*(2), 239–246. https://doi.org/10.1006/jmva.1993.1036

Milla, M., & Kudeki, E. (2006). F-region electron density and Te/Ti measurements using incoherent scatter power data collected at ALTAIR. *Annals of Geophysics*, *24*(5), 1333–1342. https://doi.org/10.1007/s00585-996-1487-3

Nygrén, T. (1996). *Introduction to incoherent scatter measurements*. Invers.

Oyama, K.-I., Balan, N., Watanabe, S., Takahashi, T., Isoda, F., Bailey, G. J., & Oya, H. (1996). Morning overshoot of Te enhanced by downward plasma drift in the equatorial topside ionosphere. *Journal of Geomagnetism and Geoelectricity*, *48*(7), 959–966. https://doi.org/10.5636/jgg.48.959

Oyama, K.-I., Watanabe, S., Su, Y., Takahashi, T., & Hirao, K. (1996). Season, local time, and longitude variations of electron temperature at the height of 600 km in the low latitude region. *Advances in Space Research*, *18*(6), 269–278. https://doi.org/10.1016/0273-1177(95)00936-1

Papoulis, A. (1984). *Probability, random variables, and stochastic processes*. McGraw-Hill.

Pfaff, R., Rowland, D., Freudenreich, H., Bromund, K., Le, G., Acuña, M., & Wilson, G. R. (2010). Observations of DC electric fields in the low-latitude ionosphere and their variations with local time, longitude, and plasma density during extreme solar minimum. *Journal of Geophysical Research*, *115*(A12). https://doi.org/10.1029/2010JA016023

Picone, J. M., Hedin, A. E., Drob, D. P., & Aikin, A. C. (2002). NRLMSISE-00 empirical model of the atmosphere: Statistical comparisons and scientific issues. *Journal of Geophysical Research*, *107*(A12), SIA 15–1–SIA 15–16. https://doi.org/10.1029/2002JA009430 SIA 15–16.

Pingree, J. E. (1990). Incoherent scatter measurements and inferred energy fluxes in the equatorial F-region ionosphere. PhD thesis.

Rees, M. H. (1989). *Physics and chemistry of the upper atmosphere*. Cambridge University Press. https://doi.org/10.1017/CBO9780511573118

Scherliess, L., & Fejer, B. G. (1999). Radar and satellite global equatorial F region vertical drift model. Journal of Geophysical Research, *104*, 6829–6842.

Schunk, R., & Nagy, A. (2009). *Ionospheres*. Cambridge University Press. https://doi.org/10.1017/CBO9780511635342

Shepherd, S. G. (2014). Altitude-adjusted corrected geomagnetic coordinates: Definition and functional approximations. *Journal of Geophysical Research: Space Physics*, *119*(9), 7501–7521. https://doi.org/10.1002/2014JA020264

Solomon, S. C. (2017). Global modeling of thermospheric airglow in the far ultraviolet. *Journal of Geophysical Research: Space Physics*, *122*(7), 7834–7848. https://doi.org/10.1002/2017JA024314

Solomon, S. C., Andersson, L., Burns, A. G., Eastes, R. W., Martinis, C., McClintock, W. E., & Richmond, A. D. (2020). Global-scale observations and modeling of far-ultraviolet airglow during twilight. *Journal of Geophysical Research: Space Physics*, *125*(3). https://doi.org/10.1029/2019JA027645

St-Maurice, J.-P., & Schunk, R. (1977). Diffusion and heat flow equations for the mid-latitude topside ionosphere. *Planetary and Space Science*, *25*(10), 907–920. https://doi.org/10.1016/0032-0633(77)90003-4

Stolle, C., Liu, H., Truhlk, V., Lhr, H., & Richards, P. G. (2011). Solar flux variation of the electron temperature morning overshoot in the equatorial *F* region. *Journal of Geophysical Research: Space Physics*, *116*, A04308. https://doi.org/10.1029/2010JA016235

Strobel, D. F., Young, T. R., Meier, R. R., Coffey, T. P., & Ali, A. W. (1974). The nighttime ionosphere: *E* region and lower *F* region. *Journal of Geophysical Research*, *79*, 3171–3178. https://doi.org/10.1029/ja079i022p03171

Sulzer, M. P., & González, S. (1999). The effect of electron Coulomb collisions on the incoherent scatter spectrum in the F region at Jicamarca. *Journal of Geophysical Research*, *104*(A10), 22535–22551. https://doi.org/10.1029/1999ja900025

Tapping, K. F. (2013). The 10.7 cm solar radio flux (F 10.7). *Space Weather*, *11*(7), 394–406. https://doi.org/10.1002/swe.20064

Thiemann, E. M. B., Chamberlin, P. C., Eparvier, F. G., Templeman, B., Woods, T. N., Bougher, S. W., & Jakosky, B. M. (2017). The MAVEN EUVM model of solar spectral irradiance variability at Mars: Algorithms and results. *Journal of Geophysical Research: Space Physics*, *122*(3), 2748–2767. https://doi.org/10.1002/2016JA023512

Varney, R. H. (2012). Photoelectron transport and energy balance. In *The low-latitude ionosphere* (p. 238).

Varney, R. H., Swartz, W. E., Hysell, D. L., & Huba, J. D. (2012). SAMI2-PE: A model of the ionosphere including multistream interhemispheric photoelectron transport. *Journal of Geophysical Research*, *117*(A6), 4–16.

Waldrop, L., & Paxton, L. J. (2013). Lyman α airglow emission: Implications for atomic hydrogen geocorona variability with solar cycle. *Journal of Geophysical Research: Space Physics*, *118*(9), 5874–5890. https://doi.org/10.1002/jgra.50496

Waldrop, L. S., Kudeki, E., González, S. A., Sulzer, M. P., Garcia, R., Butala, M., & Kamalabadi, F. (2006). Derivation of neutral oxygen density under charge exchange in the midlatitude topside ionosphere. *Journal of Geophysical Research*, *111*(A11), A11308. https://doi.org/10.1029/2005JA011496

Yang, T., Park, J., Kwak, Y., Oyama, K., Minow, J. I., & Lee, J. (2020). Morning overshoot of electron temperature as observed by the swarm constellation and the international space station. *Journal of Geophysical Research: Space Physics*, *125*(2). https://doi.org/10.1029/2019ja027299

Zoennchen, J. H., Nass, U., & Fahr, H. J. (2015). Terrestrial exospheric hydrogen density distributions under solar minimum and solar maximum conditions observed by the TWINS stereo mission. *Annals of Geophysics*, *33*(3), 413–426. https://doi.org/10.1029/2011ja017280